






RESEARCH ARTICLE | MARCH 04 2024

## Displacement of hypersonic boundary layer instability and turbulence through transpiration cooling

Philipp Kerth ; Laurent M. Le Page ; Sebastien Wylie; Raghul Ravichandran ; Andrew Ceruzzi ; Benjamin A. O. Williams ; Matthew McGilvray



*Physics of Fluids* 36, 034102 (2024)

<https://doi.org/10.1063/5.0189321>

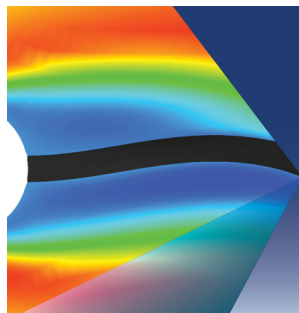


View  
Online



Export  
Citation

02 May 2024 12:57:40



## Physics of Fluids

Special Topic:

### Fluid-Structure Interaction

Guest Editors: A-Man Zhang, Tiegang Liu, Boo Cheong Khoo and Nhan Phan-Thien

[Submit Today!](#)

# Displacement of hypersonic boundary layer instability and turbulence through transpiration cooling

Cite as: Phys. Fluids **36**, 034102 (2024); doi: 10.1063/5.0189321

Submitted: 28 November 2023 · Accepted: 5 February 2024 ·

Published Online: 4 March 2024



View Online



Export Citation



CrossMark

Philipp Kerth, Laurent M. Le Page, Sebastien Wylie, Raghul Ravichandran, Andrew Ceruzzi, Benjamin A. O. Williams, and Matthew McGilvray

## AFFILIATIONS

Department of Engineering Science, University of Oxford, Oxford OX2 0ES, United Kingdom

<sup>a)</sup> Author to whom correspondence should be addressed: laurent.lepage@eng.ox.ac.uk

## ABSTRACT

Hypersonic boundary-layer transition onset is commonly characterized in wind tunnel experiments by measuring the surface heat transfer rise above the laminar level. Techniques such as infrared thermography and thin film gauges are routinely used in the field. However, when an interfering cooling effect is present due to foreign gas transpiration, these methods are known to be inadequate. This study uses a 7° half-angle cone at Mach 7 with helium or nitrogen injection through a porous segment within the model frustum. The injector spans 60° in azimuth and is located 300 mm from the sharp nose tip, close to the onset of natural boundary-layer transition. Nitrogen and helium injection reduce the surface heat flux below the laminar level for up to 50 mm downstream of the injector. Comparisons to schlieren images and pressure measurements indicate an advance of transition. Optical diagnostics reveal how instabilities are pushed away from the model surface by the injected gas. This is found through spectral analysis of schlieren images and focused laser differential interferometry signals, which revealed further information about how inaccuracies of detecting transition with surface gauges under the influence of transpiration cooling originate.

© 2024 Author(s). All article content, except where otherwise noted, is licensed under a Creative Commons Attribution (CC BY) license (<http://creativecommons.org/licenses/by/4.0/>). <https://doi.org/10.1063/5.0189321>

## I. INTRODUCTION

While a reentry vehicle descends through Earth's atmosphere along its trajectory, boundary-layer transition may not be present at high altitudes, but upon increasing density and Reynolds number, turbulence will eventually move forward on the geometry with drastic aerothermodynamic consequences.<sup>1,2</sup> Driven by the need of prediction methods and design tools, as well as fundamental research ambitions,<sup>3</sup> more needs to be understood about the fluid physical mechanisms causing said process.<sup>4</sup>

Despite suffering from higher noise levels compared to free flight, wind tunnel measurements are still an integral component of this research.<sup>4–6</sup> In these facilities, researchers commonly utilize the connection of turbulence with aerodynamic friction and hence heat transfer<sup>7</sup> to determine the transition location.<sup>8</sup> Techniques such as infrared thermography,<sup>9,10</sup> thermocouples,<sup>8,11</sup> thin film gauges,<sup>12,13</sup> atomic layer thermopiles (ALTP),<sup>14,15</sup> and temperature sensitive paint<sup>16</sup> are used in the field to infer instability data or laminar-turbulent transition from surface heat flux recordings. However, when a cooling technique

is present, surface instruments are evidently subject to coolant and boundary layer gas simultaneously and may therefore be unable to accurately resolve turbulent heating. Use of hot wires<sup>17–19</sup> may eliminate such ambiguities, but those probes have severe limitations in hypersonic flow environments due to their fragility and invasive nature.<sup>20</sup> Optical techniques such as schlieren imaging are also capable of resolving instability waves and turbulent flow; however, they do not deliver measurements at the model surface. Instabilities are often studied with differential pressure gauges (see, e.g., Estorf *et al.*<sup>21</sup>), but those may suffer from the same ambiguities with gas transpiration as they are also flush mounted at the surface.

The arbitrariness of experimentally determining the transition location has been extensively discussed in the literature.<sup>4</sup> Schneider highlights<sup>4</sup> that transition is a process along a certain region. He subsequently argues that describing transition as a precise line on a vehicle will thus strongly rely on the criterion chosen by the researcher.<sup>4</sup> Addressing the said problem more than 40 years ago, Pate<sup>22</sup> concludes: “When conducting transition studies at least two methods should

always be used. Optical methods (schlieren, shadowgraph) often provide a satisfactory second technique.<sup>22</sup>

Due to strong heating effects in the hypersonic speed regime,<sup>23</sup> active cooling has been of interest for decades, which is evident when considering how Refs. 24–26 discuss studies distributed across more than 60 years. If gas is transpired out of the wall, it will impact transition.<sup>11,24,25</sup> Moreover, the state of the boundary layer also influences the cooling quality.<sup>27</sup> Transpiration cooling runs at risk of advancing transition<sup>25</sup> which was discovered in the 1950s.<sup>26</sup> Under certain circumstances, if the blowing ratio is small enough, gas transpiration can lead to the desired reduction in skin friction (see, e.g., Refs. 28 and 29). For example, the measurements from Tanno *et al.*<sup>28</sup> show that gas transpiration can quickly cause the opposite effect and increase surface heating because of transition. Due to this undesired effect, understanding the detection of transition under the influence of active cooling is a high priority.

Schneider<sup>25</sup> particularly criticizes a study by Dunavant and Everhart,<sup>30</sup> for not sufficiently incorporating the heat mitigation effect of injection into their analysis method of heat flux data. He therefore brands their transition results as “subject to interpretation.”<sup>25</sup> He writes that their transition locations are nearly impossible to determine from the given data, as it is unclear how much cooling affected those measurements.

Two more recent studies conducted on cones with gas injection both experimentally inferred transition from surface thermocouple data.<sup>14,31,32</sup> For Jewell *et al.*,<sup>11,31</sup> injection occurred close to the apex, and transition was determined via an intermittency method.<sup>31,33</sup> In contrast, Camillo *et al.*<sup>14</sup> delivered coolant to the boundary layer via a narrow porous injection segment in the direct vicinity of transition on their cone model. They acknowledge the problem of having cooling and transition present in the same area while attempting to capture a heat transfer increase due to beginning turbulence. Their method to infer transition onset is based on comparing theoretically obtained laminar heat flux levels to averaged thermocouple data.<sup>14</sup>

Work by Kerth *et al.*<sup>34</sup> has dealt with a similar gas injection scenario, wherein transition was inferred from schlieren images and thin film gauges. Hereby, transition took place far away from the injection location. The porous nose injector segment ended at an axial distance of 58 mm, while transition occurred around 350 mm at  $Re_u = 18 \times 10^6 \text{ m}^{-1}$ . It was thus assumed that the cooling effect had largely subsided, and observed heat flux reductions were predominantly due to a delay in transition. Accordingly, schlieren, surface pressure, and heat flux measurements were all in good agreement with respect to boundary layer stability results.<sup>34</sup> It is however assumed that the contrasting injector location in the work presented below—a porous segment within the cone frustum near the location of natural transition—introduces a significantly more complex flowfield. This makes it harder to obtain physical quantities to infer any interpretation about the local stability state of the boundary layer.

Stalmach *et al.*<sup>3</sup> discussed the problem of measuring transition location with cooling in great detail. Among other aspects, they specifically highlight discrepancies in between optics (shadowgraph in their case) and surface heat transfer. Stalmach *et al.*<sup>3</sup> acknowledge how especially heat transfer measurement locations and subsequently their interpretation for transition results are influenced by the coolant gas. It needs to be mentioned here how the geometry of their injector deviates significantly from the presented example below. Their nearly entirely

porous cone will have caused thin film gauges to always be influenced by the proximity of gas injection.

Because porous injectors are used for transpiration experiments, roughness is always present to some extent. There are known cases where roughness has been utilized to achieve a transition delay in hypersonic conditions,<sup>35</sup> but altering this circumstance can also yield the opposite result.<sup>36</sup> It is therefore impossible to exclude that the roughness from the model used in this study had an effect. Nevertheless, only one model with no change in experimental configuration except for the gas injection is used in this work, ensuring comparability of test cases.

It is well known, for example, from Stalmach,<sup>3</sup> Laganelli and Martelluci,<sup>37</sup> Marvin and Akin,<sup>38</sup> and many other studies with gas injection,<sup>25</sup> that surface instrumentation cannot reliably detect transition when influenced by transpiration cooling. Here, we aim to focus our experimental investigation on fluid mechanical effects of gas injection on the boundary layer closely downstream of a locally confined transpiration cooling surface on a hypersonic, conical geometry. Because of the central injector segment, it is possible to observe how existing boundary layers respond to different injection scenarios. We extend parts of Camillo *et al.*'s<sup>14</sup> research with a different coolant, helium, and test in a low enthalpy environment, yet with a similar geometry and Mach number, focusing specifically on small scale effects near the injector. Helium demonstrates enhanced cooling efficiency compared to nitrogen at equivalent transpiration mass flux per unit area, as evidenced by experimental studies by Gülhan and Braun,<sup>24</sup> and Naved *et al.*<sup>39</sup> Additionally, it exerts a more significant influence on the boundary layer thickness, as highlighted by Ifti *et al.*<sup>40</sup> This comparison aims to enhance our understanding of the interplay between turbulence, injection, and instability. The objective is to contribute further experimental insight into the fluid physical effects of transpiration cooling on boundary-layer transition in the immediate vicinity of the injector.

## II. EXPERIMENTAL SETUP

### A. Test model with gas injection

The 7° half-angle cone, shown in Fig. 1, has been previously employed in the same configuration and injector by Kerth.<sup>41,42</sup> The model has a straight, sharp nose tip with a nose radius smaller than 0.05 mm as given by the manufacturer and is instrumented with high frequency differential pressure sensors (PCB132A31 and PCB132B38) and in-house manufactured thin film gauges (TFG).<sup>43,44</sup> To achieve a smooth surface finish, outer radii of the model were machined with a 0.02 mm tolerance, and individual segments of the model were lathed into the outer conical shape after they were assembled. Some steps between segments have been characterized with an optical microscope. For example, the gap in between the porous injector material and the surrounding steel is around 80 μm wide.<sup>42</sup> Model dimensions and instrumentation locations can be seen in Fig. 1. 0° angle of attack and yaw is maintained for all tests with ±0.1° uncertainty. The method is based on comparing the second mode wave spectra on four differential pressure gauges at 45°, 135°, 225°, and 315° around the cone.<sup>42,45</sup> When the characteristics of the oscillation spectra match at each sensor, the cone is considered aligned. This ensures that the reference for alignment is not the mounting, nozzle, or test section, but exclusively the free stream of the tunnel and the associated instability progress along the cone. Microporous aluminum BF100Al<sup>46</sup> is used to transpire

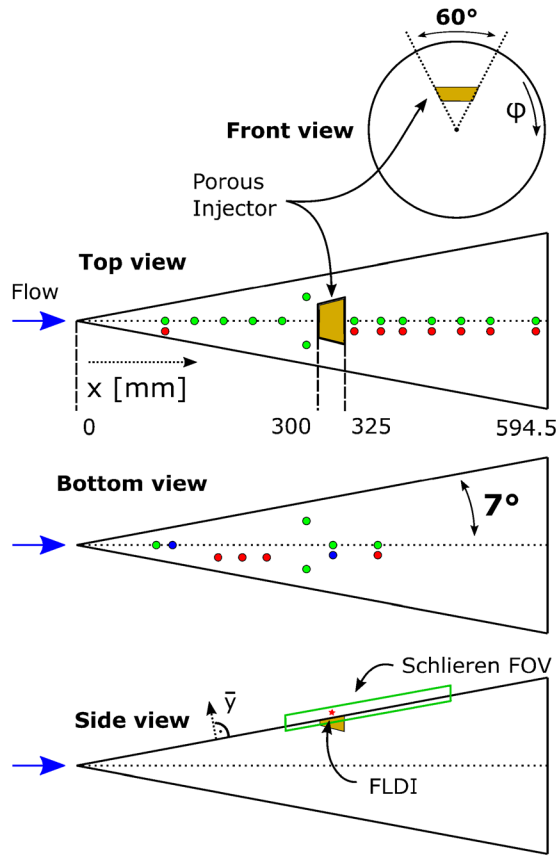


**FIG. 1.** Test model geometry. Blue points represent absolute pressure gauges, red are thin film gauges, and green PCB high frequency pressure transducers. The porous injector patch is marked in yellow, which spans a 60° azimuth.  $\bar{y}$  is the wall normal coordinate. Figure with permission from Kerth, “Effect of transpiration cooling on boundary layer transition for hypersonic flight,” Ph.D. thesis (University of Oxford, 2022).<sup>42</sup>

gas into the boundary layer, which has a mean pore diameter of 30–40  $\mu\text{m}$ .<sup>47</sup> The injector section is located 300 mm from the sharp tip, is 60° wide, and indicated as a yellow surface is Fig. 1. A plenum below the 10 mm thick porous wall allows measurement of the plenum pressure using a Kulite XT-190S(M). Gas flow through the porous injector is controlled using an Omega FMA2611A mass flow controller. Before the campaign, a curve of mass flow rate vs plenum pressure is recorded. Due to the radial 10 mm thickness, the Darcy and Forchheimer coefficients of the porous material patch can be determined using the Nelder–Mead simplex search algorithm, applied to the aforementioned curve.<sup>48,49</sup> The Darcy-coefficient is  $K_D = (8.26 \pm 0.04) \times 10^{-14}/\text{m}$ , and the Forchheimer-coefficient is  $K_F = (5.3 \pm 0.1) \times 10^{-10}/\text{m}^2$ . The blowing ratio is then computed via

$$F = \frac{\dot{m}_c}{\rho_e u_e A}. \quad (1)$$

Herein, we employ the same method as in Kerth *et al.*<sup>41,42</sup> to obtain the relevant physical input parameters. Using the HDT freestream properties and the geometry as an input, we assume that the

approximation for the Taylor–Macoll solution<sup>50,51</sup> delivers a reasonable estimate for the boundary-layer edge Mach number. We subsequently obtain the boundary-layer edge velocity and then the density through ideal gas relations, which is determined for the denominator of Eq. (1). The numerator is obtained through a Darcy–Forchheimer computation using the measured plenum pressure and the previously obtained material coefficients.

Similarly to Ifti *et al.*,<sup>48</sup> Miró *et al.*,<sup>10</sup> Dittert *et al.*,<sup>52</sup> and with the same procedure as presented by Kerth *et al.*<sup>41,42</sup> the outflow profile of the injector patch was measured using a 1 mm wide Dantec Dynamics 55P11 hot wire probe. After collecting the data presented by Kerth *et al.*,<sup>41,42</sup> the model had been disassembled and partially refurbished. In an attempt to investigate the reproducibility of said effusion characteristics, we repeat the outflow measurement procedure. Using a traverse arm, the porous 3D segment’s outflow distribution was scanned at a distance of  $(1.5 \pm 0.5 \text{ mm})$  from the injector surface, using a hot wire probe. The result is plotted as a velocity map in Fig. 2, showing no leaks at the interfaces of porous aluminum and impervious steel. The presented flow velocity measurement does not represent the actual outflow speed from microscopic pores. The hot wire is too large, and its distance from the porous material was too far in order to resolve such features. Macroscopic outflow hotspots or leaks could only be located with an accuracy in the  $\sim 2 \text{ mm}$  range.

### B. Surface instrumentation

Like other surface sensors in high-speed flow experiments, PCB 132A31 and 132B38 piezoelectric sensors are flush mounted in the instrumentation hole locations shown in Fig. 1 using RTV silicone. The sensor locations are additionally given in the Table I below.

Using the manufacturer calibration, the signals are converted from voltage to pressure and then normalized by the mean cone surface pressure for the relevant flow condition. A sampling rate of

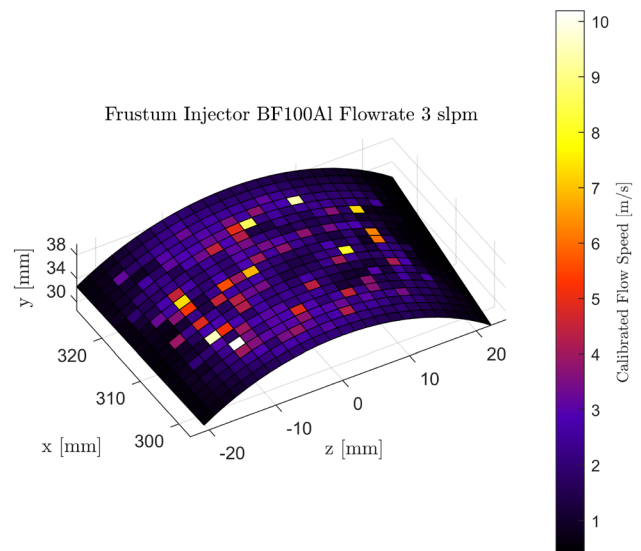


**FIG. 2.** Injector effusion map. Figure with permission from Kerth, “Effect of transpiration cooling on boundary layer transition for hypersonic flight,” Ph.D. thesis (University of Oxford, 2022).<sup>42</sup>

**TABLE I.** Model sensor locations.<sup>41,42</sup> The coordinates refer to the coordinate system defined in Fig. 1 taken from Kerth, "Effect of transpiration cooling on boundary layer transition for hypersonic flight," Ph.D. thesis (University of Oxford, 2022).<sup>42</sup>

x-coordinate	Azimuthal ( $\phi$ ) coordinate	Sensors instrumented
127.0 mm	0°	PCB
147.0 mm	0° and 15°	PCB and TFG
175.0 mm	0° and 195°	PCB and TFG
203.0 mm	0° and 195°	PCB and TFG
231.0 mm	0° and 195°	PCB and TFG
262.0 mm	0°	PCB
282.0 mm	45°, 135°, 225°, and 315°	PCB
338.0 mm	0° and 15°	PCB and TFG
358.0 mm	0° and 15°	PCB and TFG
383.7 mm	0° and 15°	PCB and TFG
408.7 mm	0° and 15°	PCB and TFG
433.8 mm	0° and 15°	PCB and TFG
458.7 mm	0° and 15°	PCB and TFG
488.7 mm	0° and 15°	PCB and TFG
533.7 mm	0° and 15°	PCB and TFG

2 MHz allows the calculation of Welch’s power spectral density estimate at suitably high frequencies<sup>53,54</sup> for our current analysis aims.

We obtain surface Stanton number values from the following Eq. (2), where  $\dot{q}$  is the heat flux from the thin film gauges (TFG),  $c_p$  is the tunnel test gas heat capacity,  $T_r$  is the recovery, and  $T_w$  is the wall temperature:

$$St = \frac{\dot{q}}{\rho_e u_e c_p (T_r - T_w)}. \tag{2}$$

$T_r$  is hereby obtained using the following expression:

$$T_r = T_e(1 + r((\gamma - 1)/2)M_e^2), \tag{3}$$

where  $r$  is the square root of the Prandtl number for laminar flow and the cube root of the Prandtl number for turbulent flow.

Point measurements on the cone surface are obtained using thin film gauges,<sup>43,44</sup> distributed along the axial length of the cone, as shown in Fig. 1. Oldfield’s<sup>55</sup> processing methods allows conversion of voltages sampled at 125 kHz into heat flux data. The procedure performs a deconvolution of the measured temperature time series, to obtain the underlying heat flux. Oldfield<sup>55</sup> hereby calculates the impulse response by generalizing the analytical solution for the temperature profile originating from a discrete step in heat flux.

At  $x = 433.7$  and  $x = 147$  mm, we compensate the heat flux values for gauge surface deformities by employing constant correction factors, which were in turn obtained from comparing the gauge’s response to Eckert correlations.<sup>56–58</sup>

Those correlations are also used to compare measured heat flux values in Fig. 5.

### C. Flow conditions

The cone model was placed in the test section of a Ludwieg tube, namely, the Oxford Thermofluid Institute’s High Density Tunnel

(HDT).<sup>59–61</sup> More information about the facility, the working principle, and previous experiments with similar models can be found in the references given above. The flow properties of the tested flow condition here can be found in Table II. Where  $T_0$  is the total temperature,  $M_\infty$  is the freestream Mach number,  $T_\infty$  is the freestream temperature,  $Re_u$  is the freestream unit Reynolds number,  $p_\infty$  is the freestream pressure,  $p_0$  is the stagnation pressure,  $u_\infty$  is the freestream velocity, and  $\mu_\infty$  is the freestream viscosity.

When the Oxford HDT was commissioned, several parameters were measured for the facility and are now used as inputs for condition computations. The initial parameters are the total temperature profile<sup>62</sup> and the Pitot-pressure profiles. For every shot, a sensor records the nozzle stagnation pressure with the same sampling rate as all other instrumentation. By using standard expressions for hypersonic conditions, all quantities are derived from those three initial parameters, the nozzle area ratio, and Keyes<sup>63,64</sup> viscosity model.<sup>42</sup>

The uncertainties were obtained through standard error propagation methods. For the computation of the Mach number and the Darcy- and Forchheimer-coefficient, this was not possible as they were obtained through iterative procedures. Hence, a Monte Carlo method was used to calculate the uncertainty.<sup>42</sup>

### D. Z-type Schlieren

A z-type schlieren system<sup>65,66</sup> is used to observe the boundary layer by capturing cone-surface normal density gradients. The narrow field of view extends along the center of the cone and is inclined by 7° as visible in Fig. 1. Data processing steps are very briefly summarized here: Precautions were taken to remove distortions of the images and locate the field of view relative to the cone. Both are achieved by recording a checkerboard mounted to the cone prior to closing the tunnel test section. We subsequently subtract an averaged background image and apply a gamma correction with MATLAB’s *imadjust* function. In the results presented below, further processing steps enable assessment of optically measured frequency content. For optimal comparability, power spectral density (PSD) spectra are calculated with the same procedure as for PCB sensors directly for each pixel over a range of 2000 frames. Every pixel is herein treated as an independent time series of schlieren signal intensities,  $I(t)$ , sampled at a 700 kHz frame rate. As the sampling frequency and number of data points is lower compared to the surface instrumentation, the Hann windows is adapted according to 200 points in length.

**TABLE II.** HDT condition.

Property	Value	68% confidence interval
$T_0$ (K)	460	15
$M_\infty$	7.00	0.03
$T_\infty$ (K)	43	1.5
$Re_u$ ( $10^6$ /m)	12.8	0.7
$p_\infty$ (Pa)	520	15
$p_0$ (kPa)	2160	80
$u_\infty$ (m/s)	915	10
$\mu_\infty$ ( $10^{-6}$ Pas)	3.0	0.1

**E. Focused laser differential interferometry (FLDI)**

The idea for this “non-imaging common path interferometer”<sup>67</sup> is more than 50 years old,<sup>68</sup> and the system has since proven its capability to conduct measurements in hypersonic flow fields and associated boundary layers<sup>67,69</sup> (see also e.g., Refs. 70 and 71). The Oxford FLDI largely follows the setups described by Smeets,<sup>68</sup> Schmidt *et al.*,<sup>69</sup> or Fulghum,<sup>67</sup> except with a few components added to match spatial constraints. It first consists of a Ventus 550 mW 671 nm continuous wave laser (A) (Fig. 3 and Table III) whose beam is divided into two of orthogonal polarizations using a Wollaston prism (G) with a 2 arc min splitting angle, alike the original setup proposed by Smeets.<sup>68</sup> A biconvex lens (H) subsequently focuses the separated beams.<sup>69</sup> This generates what would be described as “depth-of-field” in a camera<sup>72</sup> and hence concentrates the sensitivity of FLDI in a narrow field in beam wise direction.<sup>67,68,71</sup> Herein, focal lengths of the lenses were specifically selected to match the width of the HDT’s test section. Two adjustable mirrors (I) turn the beam by 90° twice to save space next to the test section windows, giving the Oxford FLDI a z-shaped light path. Said mirrors are finely adjustable and allowed precise alignment of the beam to the model. Similarly, the optical rails on both sides of the tunnel were mounted on Thorlabs LJ750/M lab jacks enabling high precision vertical positioning ( $\pm 5 \mu\text{m}$ ) of the interferometer’s measurement point.

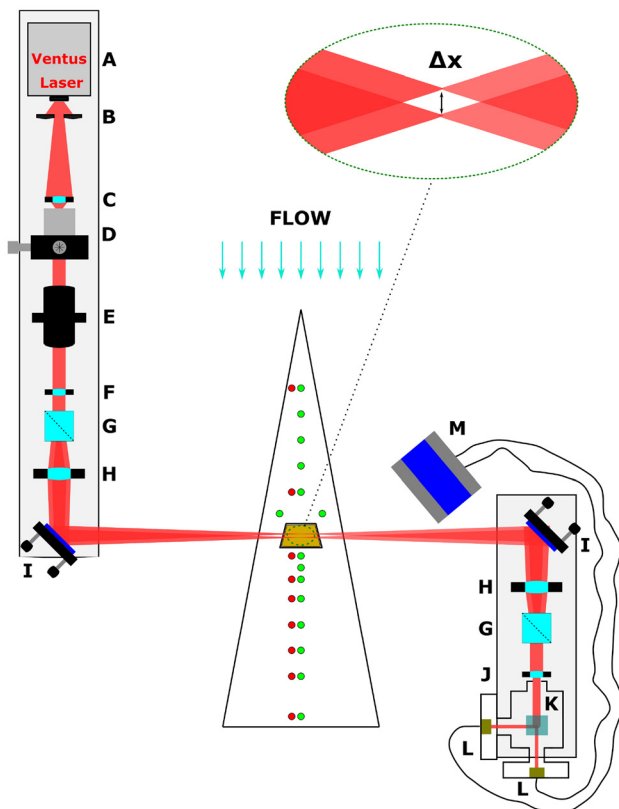


**FIG. 3.** FLDI setup. The components can be found in Table III. Figure with permission from Kerth, “Effect of transpiration cooling on boundary layer transition for hypersonic flight,” Ph.D. thesis (University of Oxford, 2022).<sup>42</sup>

**TABLE III.** FLDI components.

Component	Description
A	Laser Quantum Ventus 671
B	Iris aperture
C	Achromatic doublet lens
D	Pinhole + Achromatic doublet lens
E	Faraday isolator with linear polarizer
F	Aspheric lens $f = 10 \text{ mm}$
G	Birefringent Wollaston prism
H	Biconvex lens $f = 100 \text{ mm}$
I	Adjustable mirror
J	45°—polarizer
K	Polarizing beam splitter
L	Photodiode
M	Picoscope with differential port

Alike schlieren systems, FLDI utilizes the Gladstone-Dale relation, which links gas density and refractive index.<sup>67–69,73</sup> The optical principle of said interferometer allows metrological access to refractive index fluctuations by comparing polarization states of the two independent paths within the test volume,<sup>67–69</sup> which is achieved using two photodiodes (L) and a differential port connected to an oscilloscope (M). In good agreement with the values from Ceruzzi,<sup>71</sup> the beam separation at the point of focus has been determined to be  $(64 \pm 7) \mu\text{m}$  using a Thorlabs BC106N-UV/M beam profiler. More information about the technique’s general working principle can be found in the original publication from Smeets<sup>68</sup> or in theses from Fulghum,<sup>67</sup> Parziale,<sup>70</sup> or Ceruzzi.<sup>71,74</sup>

**1. Recording and alignment procedure**

FLDI data acquisition was run for 20 ms and sampled with an oscilloscope at 10 MHz, while the laser was run at full power during a tunnel shot. The trigger signal for the recording was set to match the start of the desired steady state conditions in the HDT.

Alignment of the system was conducted by shining the focused laser spot onto a semi-transparent checkerboard, which was in a fixed position relative to the cone above the injector, and orthogonal to the FLDI beam direction. A photograph of the focal point, cone edge, and checkerboard was then taken with a SLR camera. Using MATLAB inbuilt functions,<sup>75</sup> the checkerboard of 1 mm square size is used to relate pixel ( $px$ ) to spatial coordinates. The cone edge, and known position of the checkerboard relative to the cone, then allow the calculation of the laser spot location in the coordinate system of  $x$  and  $y$  as defined in Fig. 1.

**2. Depth of field of FLDI setup**

As described previously, a particular asset of such laser interferometers is their narrow depth of field. Similarly to Ceruzzi *et al.*,<sup>74</sup> we have characterized the system’s response by translating an acoustic fluctuation source along the beams length. Here, this is not a gaseous jet as in Ref. 74, but a Multicom Pro 300 kHz sound transceiver, which was driven by a function generator. It is mechanically traversed

along the FLDI light path around the sensitive region in a benchtop investigation at room temperature and atmospheric pressure. Using the same acquisition procedure and sampling as described in Sec. II E 1, voltages were acquired for 19 locations spaced evenly along the beam path. PSDs were calculated for each recording, and the value at 300 kHz was then plotted against the coordinate along the beam  $z$  [see blue points in Fig. 4(a)]. A Gaussian fit provides an estimate for the full width half maximum (FWHM) at around 43 mm or the standard deviation,  $\sigma \approx 18$  mm.

Several recent publications discussed the depth-of-field of FLDI in more detail with some particularly focusing on its ability to penetrate turbulent environments around an object of interest.<sup>70,74,76,77</sup> All those sources reveal dependencies of the depth-of-field on the frequency, wavelength, and amplitude of density disturbances within the probed flowfield. Therefore, additional post-processing steps need to be added to investigate the performance of the Oxford FLDI system as it is not possible to simply compare the FWHM of the sensitivity at 300 kHz to the beam-wise width of the boundary layer.

### 3. Frequency and wavelength dependent response of Oxford FLDI

Frequency and wavelength of the second mode could not be matched simultaneously during the benchtop test at room temperature seen in Fig. 4(a), as the FLDI's response depends on both parameters.<sup>70,74,76,77</sup> A 300 kHz frequency correspond to  $\lambda \approx 1.1$  mm sound wavelength at standard conditions, whereas the second mode wavelength is around 2.5 mm in the relevant tunnel flow,<sup>42</sup> rendering the FWHM from the Gaussian fit above imprecise. Ceruzzi and Cadou<sup>74</sup> present an overview of a transfer function for FLDI systems, by reproducing and combining work from Parziale *et al.*<sup>70,78</sup> and Schmidt and

Shepherd.<sup>69</sup> The proportionalities in the transfer function suggest that the sensitive field of the FLDI system is considerably larger and the maximum sensitivity substantially lower at  $\lambda = 2.5$  mm than at  $\lambda = 1.1$  mm, where it was characterized. We therefore present a procedure to indirectly infer the FLDI's response at  $\lambda = 2.5$  mm.

For the transfer function, we combine mathematical formulations from Parziale *et al.*<sup>70,78</sup> and Ceruzzi and Cadou<sup>74</sup> and use

$$T = \sin\left(\frac{\pi s_b}{\lambda}\right) \exp\left[\frac{\left(\frac{2\pi}{\lambda}\right)^2 d_b}{8} \left(1 + \left(\frac{\lambda_1 z}{\pi d_b^2}\right)^2\right)\right]. \quad (4)$$

The full transfer function,  $T$ , across  $\lambda$ , and,  $f$ , includes the laser wavelength,  $\lambda_b$ , the beam-wise coordinate,  $z$ , and requires knowledge of the minimum beam separation,  $s_b$ , and diameter,  $d_b = 2r_b$ . The latter value has, however, not been obtained yet for the current system. Instead, we utilize the benchtop measurement to obtain this parameter by fitting the transfer function at  $\lambda = 1.1$  mm, to the measured points from our benchtop experiment. Transfer function and PSD values were normalized with their respective maximum. This step can be seen in Fig. 4(a), where  $r_b$ , was iterated until the red curve fitted the measured blue points. We finally obtain  $r_b \approx 5.6 \mu\text{m}$ . This value is typically between 3 and 10  $\mu\text{m}$  for other FLDI setups in the literature.<sup>74,77,79,80</sup> Using this value, we calculate the transfer function and evaluate it at  $\lambda = 2.5$  mm, which predicts the FLDI depth-of-field at the relevant second mode frequency. It is plotted as the green curve in Fig. 4(a). For completeness, we re-plot Fig. 4 from Ceruzzi and Cadou<sup>74</sup> in Fig. 4(b), showing the full transfer function for the Oxford FLDI. Note that the curves for  $\lambda = 2.5$  and  $\lambda = 1.1$  mm are normalized slices through the contour plot parallel to the  $z$ -axis. Both plots demonstrate how the sensitivity spreads along a larger region as the wavelength increases.

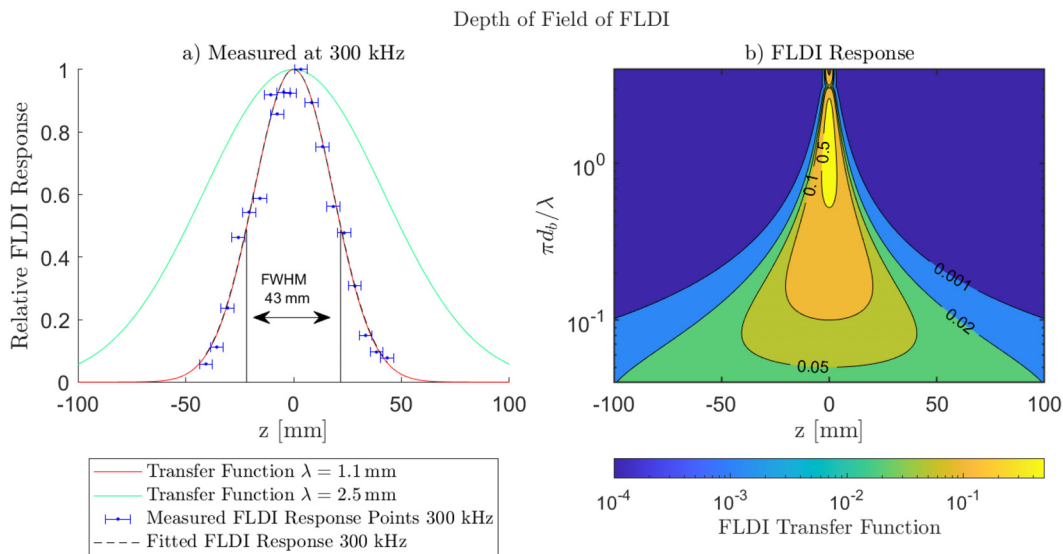


**FIG. 4.** (a) Depth of field of the FLDI setup.  $z$  is the coordinate parallel to the beam centered at the focal point of the system. Measured data for a single frequency near the expected instability are compared to the fitted transfer function and the extrapolated transfer function at the expected second mode frequency. Error bars indicate the diameter of the sound transceiver. (b) Replots Fig. 4 from Ceruzzi and Cadou<sup>74</sup> and shows the full transfer function of the FLDI.  $d_b = 2r_b$  is the beam diameter. Figure with permission from Kerth, "Effect of transpiration cooling on boundary layer transition for hypersonic flight," Ph.D. thesis (University of Oxford, 2022).<sup>42</sup>

4. Implications of FLDI response in HDT experimental setup

According to Wylie,<sup>45</sup> the core flow of HDT’s Mach 7 nozzle extends to around  $r = 130$  mm from the centerline. Wylie<sup>45</sup> obtained this value by using an array of high-frequency differential pressure transducers in the test section to analyze Pitot pressure noise levels within the tunnel flow. Up to 278 mm downstream of the nozzle exit, the given core flow radius persists and only shrinks further downstream. As the model apex pointed into the nozzle by around 100 mm, the area of interest on the cone is well within the core flow.

Figure 4(a) predicts that the instrument’s sensitivity will have decreased to less than 10% of its nominal value at only  $r = 100$  mm for the most relevant wavelength. Furthermore, HDT’s Pitot-pressure fluctuation spectra measured by PCB sensors exhibit a considerable drop in noise content at frequencies exceeding 200 kHz.<sup>45</sup> Hence, even if the sensitive region extends into the turbulent tunnel boundary layers, second mode signals at large enough amplitudes will still likely dominate. However, without further measurements about the system’s sensitivity at  $\lambda \approx 2.5$  mm, one must conservatively assume that the signal contains some freestream fluctuations.

Benitez *et al.*<sup>76</sup> used DNS to simulate a signal of interest, which was framed by turbulence. Their simulation of FLDI responses confirmed that relying on the axial diminution of its sensitivity was justified for high frequency measurements, but less acceptable for larger wavelengths and lower frequencies. Benitez *et al.*’s<sup>76</sup> simulated interferometer setup is similar to the version presented here, having the same Wollaston prisms. In contrast, the beam separation is considerably larger at  $168 \mu\text{m}$ . Benitez *et al.*<sup>77</sup> warn how fluctuations with  $\lambda > 1$  mm are “integrated across the length of the beam,”<sup>77</sup> when

analyzing another set of simulation cases. They however also report that a smaller beam separation reduces the depth-of-field, albeit at the cost of total responsiveness.<sup>77</sup> With respect to line integration, the Oxford FLDI should exhibit more favorable characteristics than the setup simulated by Benitez *et al.*<sup>76,77</sup> Furthermore, the noise spectrum of HDT does contain significantly less signal power around 300 kHz. Should, however, high frequency content at millimeter scale wavelengths be present around the nozzle core-flow, it is likely recorded to some extent by our FLDI setup.

III. EXPERIMENTAL RESULTS

A. Surface heat transfer

Figure 5 (right) plots the heat flux as recorded by thin film gauges along the cone for various injection scenarios and an uncooled case. From the references discussed in the introduction, it is clear that the surface heat-flux measurements are nearly meaningless when it comes to inferring transition under the influence of transpiration cooling. Nevertheless, those measurements are still presented here to assist in the interpretation of the presented experiments. Values measured by thin-film gauges may not hold significance for the detection of turbulence under those conditions; however, they remain pertinent in providing information on the resultant heat flux levels at the surface and, consequently, assessing the efficacy of transpiration cooling. This manuscript provides further insight into the details of why surface instrumentation is inaccurate under those circumstances beyond the aspect of heat transfer measurements.

Helium and nitrogen transpiration both successfully delay the onset of a transitional heat flux level, in agreement with Stalmach *et al.*’s<sup>3</sup> definition (the most upstream thin film gauge showing a heat

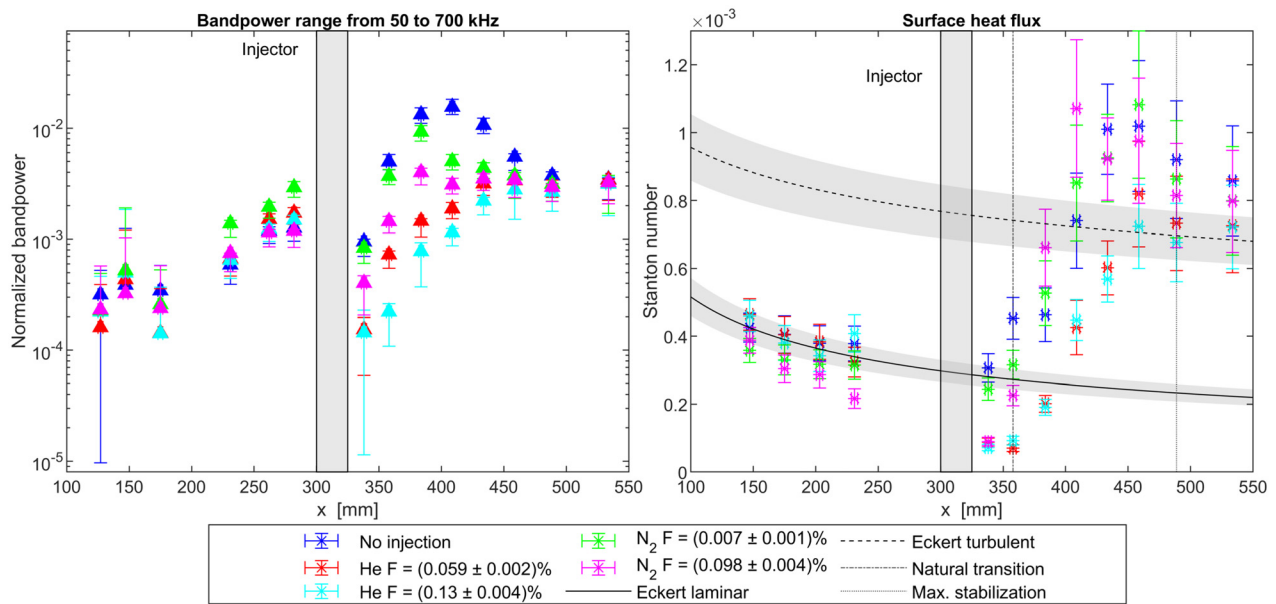


FIG. 5. Results from surface instrumentation. (left) High frequency pressure. Only the cumulative bandpower is shown in the figure. Second mode frequency peaks lie in the 280 kHz region, and hence, the first and second harmonics are included in the integrated power. (right) Heat flux distribution across the cone. Colors represent gases and injection ratios and are kept coherent across figures. Figure with permission from Kerth, “Effect of transpiration cooling on boundary layer transition for hypersonic flight,” Ph.D. thesis (University of Oxford, 2022).<sup>42</sup>

02 May 2024 12:57:40



flux significantly exceeding the laminar correlation) and similarly to the results from, e.g., Tanno *et al.*<sup>28</sup>

For those injection gases (helium and nitrogen), Fig. 5 (right) shows a reduction of heat transfer downstream of the porous patch well below the uncooled values. For nitrogen as a coolant, a fast recovery of the heat flux profile is observed: A short term reduction below the uncooled baseline is directly followed by an increase in heat transfer to uncooled levels, which is the prime example of a known shortcoming of transpiration cooling. In contrast, the given helium injection cases do not show excess heating. However, this cannot be interpreted as a transition delay.

Qualitatively, the heat transfer results from Camillo *et al.*<sup>14</sup> could be favorably compared for the nitrogen and helium injection cases in this work. An important difference hereby is the total temperature. While HEG reaches above 2800 K,<sup>14</sup> HDT does not exceed 460 K.

It remains unclear where the boundary-layer transitions to turbulence when exclusively analyzing thin film gauge measurements. A stand-alone heat flux value will contain superimposed contributions from possible turbulent frictional heating and the cooling effect.

## B. Surface pressure fluctuations

Common knowledge in the field links hypersonic boundary-layer transition on slender, 2D, axisymmetric geometries with small nose radii in low disturbance environments with growth and decay of second mode instabilities.<sup>81,82</sup> The left side of Fig. 5 summarizes all individual power spectra from Fig. 6. The bandpower values shown in Fig. 5 (left) were calculated as integrals over their respective PSDs. The frequency boundaries are chosen generously (50–700 kHz) and thus ensure inclusion of higher harmonics.

As Fig. 5 (left) indicates for the uncooled case, boundary-layer instability oscillations are first amplified before the boundary layer decays to turbulence. Landau and Lifshitz describe turbulence as “irregularly disordered”<sup>83</sup> velocity distributions. Such distributions do not show specific amplified frequencies and therefore exhibit lower total bandpower values. For all cases, the bandpower level coincides at  $x = 534$  mm, which represents the fully turbulent value. Only some cases show bandpower above the fully turbulent level, which indicates some form of modal amplification. The helium injection cases are not among them. Those show a drop even below turbulent levels of bandpower downstream of the injector. Surface pressure spectra and bandpower values downstream of the injector show no sign of modal amplification and therefore indicate a bypass mechanism<sup>81,84–86</sup> at the surface.

There is ambiguity in the state of the boundary layer further above the model surface from instrumentation measurements. From interpreting the given gauge measurements, it remains unclear how the coolant film contributes to the second mode damping or the reduction in heat transfer through gas injection. While those difficulties of surface measurements with transpiration cooling have only been reproduced from well understood examples in the literature (see, e.g., Stalmach *et al.*,<sup>3</sup> Camillo *et al.*,<sup>14</sup> and Tanno *et al.*<sup>28</sup>), we now aim to investigate in more detail how locally confined gas injection influences the wall-normal behavior of instability and turbulence using optical methods.

## C. Schlieren images

Surface instrumentation has shown reduced heating and second mode activity in the close vicinity of the model surface. Schlieren

images now provide insight whether those observations hold for the rest of the boundary layer thickness.

In Fig. 7, second mode wave packets can be observed and transition completion can be seen in the most downstream fifth of the image for nitrogen injection  $F(N_2) = 0.009\%$  and natural transition. Note that the PCB bandpower and the heat flux signals are time averages, while those single schlieren frames are not.

For  $F(He) = 0.06\%$ , full turbulence does not seem to develop until around  $x = 380$  mm for the depicted frame. Selecting one frame at random from a whole video does not capture the inherently unsteady nature of a transitioning boundary layer, but is nevertheless necessary to depict features that may remain concealed when only showing a time-averaged schlieren photograph. It is thus noted that those frames in Fig. 7 are in contrast to all spectral analysis items shown in this work, as those always represent mean flow conditions.

## D. Schlieren power spectra

Using a suitably high recording frequency and a 170 mm long high-resolution field of view allows tracking of the second mode oscillations during its growth and decay process at certain heights in the boundary layer. Like previously reported in other studies (e.g., Gülhan and Braun,<sup>24</sup> and Schmidt<sup>87</sup>), we observed a thickening of the schlieren boundary layer profile through injection. It is thus necessary to investigate whether those profile changes have repercussions on the progression of instability and turbulence. Consequently, this might provide details into the mechanisms of instability damping and heat transfer reduction at the surface. We therefore utilize the high resolution of a high-speed camera and select two pixel-paths following the cone edge at different heights above the model for plotting respective schlieren frequency spectra vs the  $x$ -coordinate. The straight yellow path in Fig. 8 follows the pixel line at the ‘natural’ edge of the boundary layer. At this height, the strongest second mode wave crests were observed upstream of the injector. For the red path (named special path in Fig. 8), ten points along the curved boundary layer edge profile were manually selected by the experimenter. The path is then calculated by linear interpolation in between all pairs of consecutive points. Finally, the lowest pixel at every  $x$ -location the path intersects with is selected and its PSD included in Fig. 8.

Above the injector, second mode power is found in the red path and no longer in the yellow. This is particularly around and downstream of  $x = 320$  mm, where more signal is present at the height of the red path in the region around 280 kHz than at the original boundary layer height. The two different paths deliver PSDs calculated from the exact same sequence of images. Only pixels at different heights were selected for the same  $x$ -locations. Therefore, it can be concluded that for the case of  $F(He) = 0.06\%$ , second mode oscillations are displaced in the wall normal direction above and downstream of the injector.

An analytical model by Ifti *et al.*<sup>40,88,89</sup> describes how a “slab”<sup>88</sup> of coolant gas forms below the original boundary layer if gas is injected from a porous surface on the model. Ifti *et al.*<sup>40,88</sup> treat those two segments as largely independent layers and assume mixing only ensues gradually driven by diffusion, provided that everything remains laminar. The findings could hence be interpreted as the coolant slab displacing air as well as instabilities away from the surface while forming the new, distended boundary layer geometry. Thus, a growth and decay process of instabilities is taking place, however not predominantly at the surface, or within the original boundary layer geometry. Surface heat flux and pressure are hence unreliable indicators for

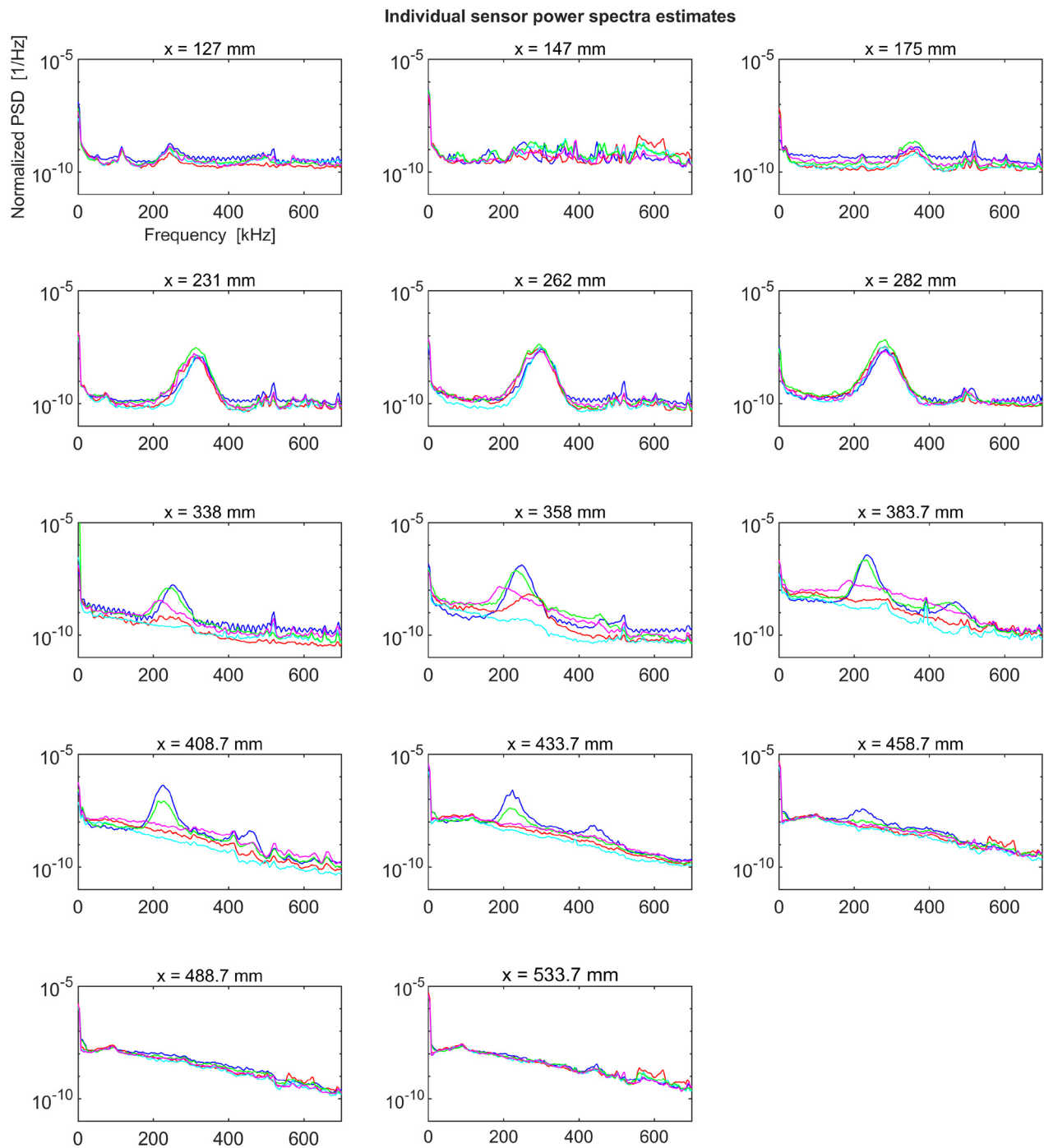


**FIG. 6.** Power spectra calculated from PCB differential surface pressure measurements used to illustrate the bandpower shown in Fig. 5. Color convention is the same as in Fig. 5. Figure with permission from Kerth, "Effect of transpiration cooling on boundary layer transition for hypersonic flight," Ph.D. thesis (University of Oxford, 2022).<sup>42</sup>

spatial progression of boundary layer stability with injection. They cannot measure effects in the displaced air boundary layer.

For the close downstream vicinity of the injector, boundary layer thickening observed in schlieren and analytical predictions by Ifiti<sup>40,88</sup> match

reasonably. For  $F(\text{He}) = 0.04\%$ , the height of the coolant slab is projected as  $h(\text{He}) \approx 0.6 \text{ mm}$  and for  $F(\text{He}) = 0.1\%$   $h(\text{He}) \approx 1.2 \text{ mm}$ . In the shown schlieren images, the boundary layer thickens by approximately 0.85 and 1.16 mm, respectively. For the nitrogen case with  $F = 0.01\%$ , an

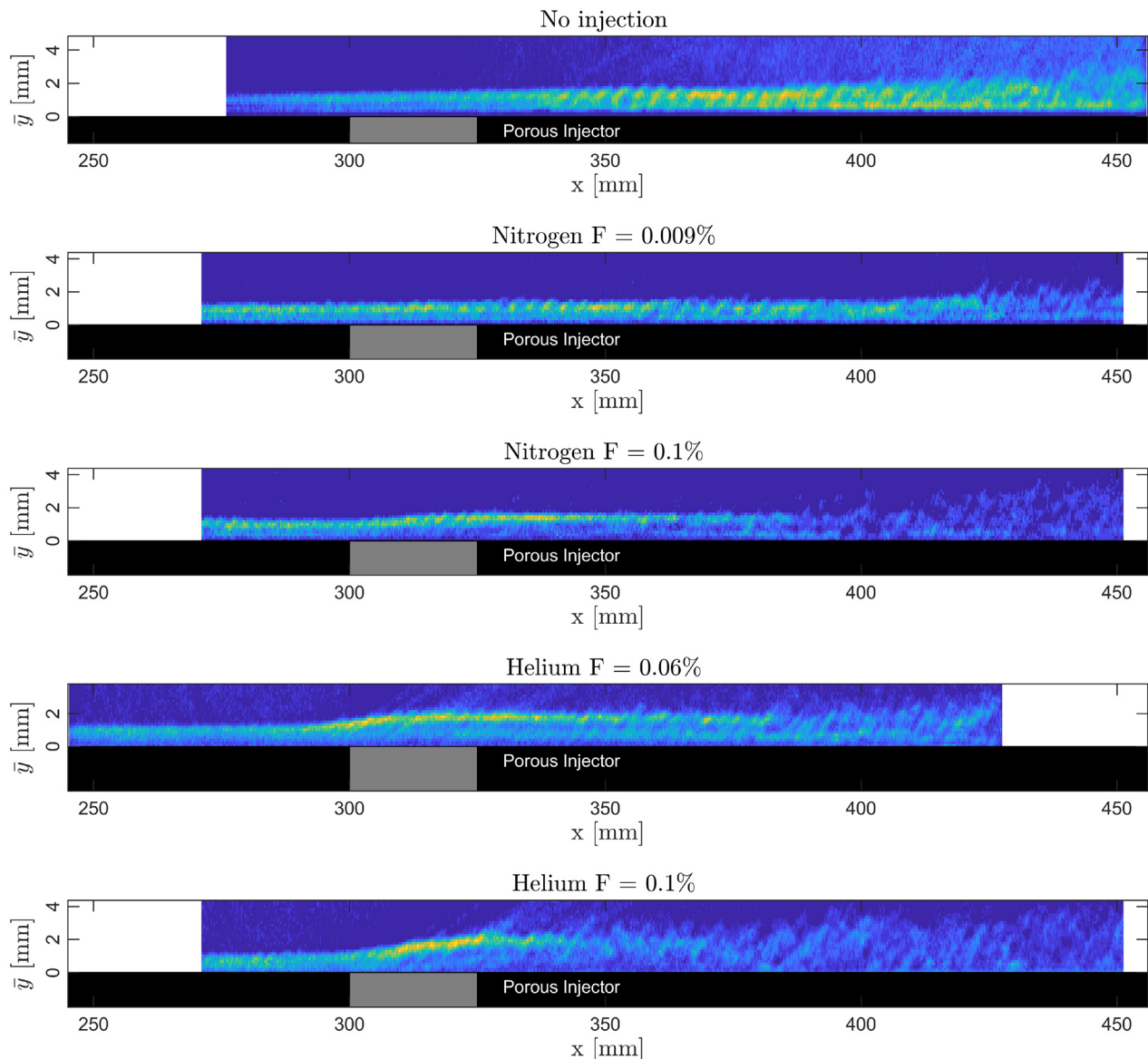


**FIG. 7.** Single schlieren frames of shots with and without injection. The injector is marked in the images. Images are not to scale in width and height. Figure with permission from Kerth, "Effect of transpiration cooling on boundary layer transition for hypersonic flight," Ph.D. thesis (University of Oxford, 2022).<sup>42</sup>

increase in height was below the pixel resolution. Surface pressure spectra show how the second-mode power is reduced at the surface for helium injection. Figure 8 now suggests that most of the second mode power is not reduced across the whole visualized boundary layer thickness. The second-mode waves are pushed above the surface by the coolant injection. In addition, a visible second layer forms below the original boundary layer gas, when considering the schlieren frames in Sec. II and Fig. 7.

### E. Frequency shift within boundary layer

Kerth<sup>41,42</sup> characterized the frequency shift of second modes with injection of different gases, similarly to Schmidt.<sup>87</sup> While Schmidt<sup>87</sup>

investigated Mach 4 flow deducting the frequency shifts from schlieren measurements, Kerth *et al.*<sup>41,42</sup> conducted their experiments at Mach 7 using high frequency surface pressure measurements. It was found by both that higher injection rates lead to a stronger reduction in frequency.

Research by Wylie *et al.*<sup>45,61</sup> suggests that transition in HDT is dominated by second modes for the given sharp and slender cone geometry and the Mach 7 nozzle, the underlying stability physics might differ from Schmidt *et al.*<sup>87</sup> Surface instruments have been found to be unreliable in measuring the second mode downstream of an injector in previous sections. It is thus critical to determine whether the frequency shift observed by Kerth *et al.*<sup>41,42</sup> is only an effect of the

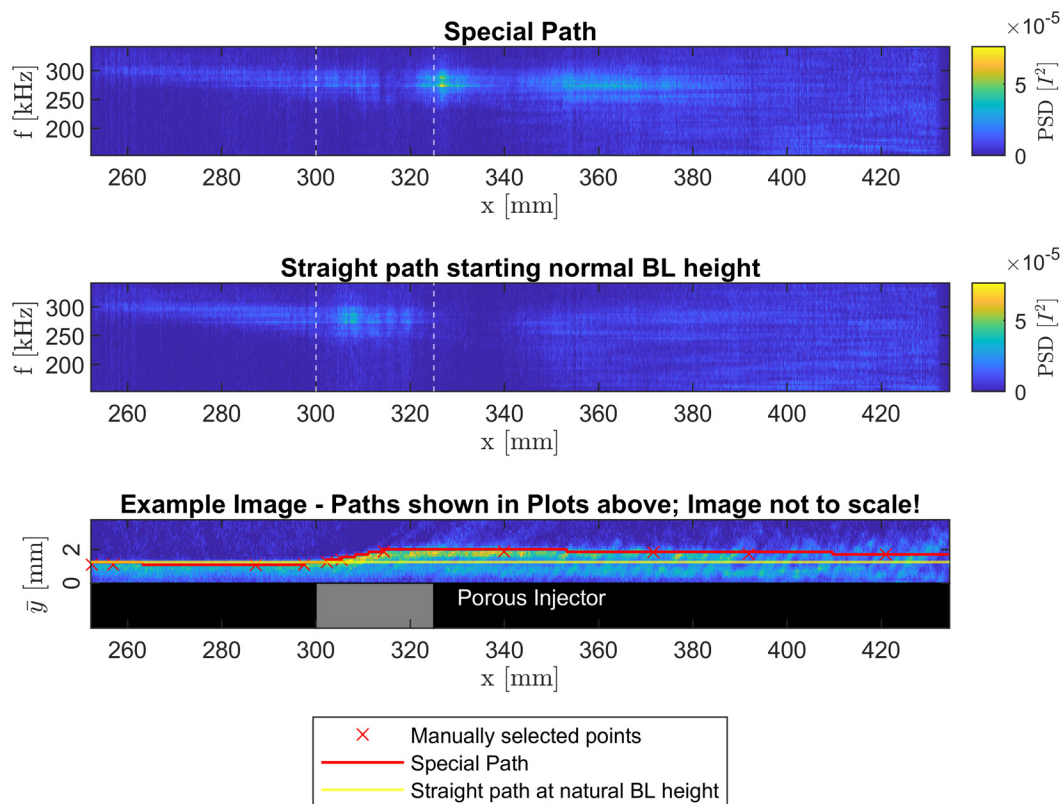


**FIG. 8.** Power spectra maps of schlieren images. The PSD is calculated for every pixel along the shown paths. Power is represented in the colorscale. Both power spectra along the paths are calculated with the same procedure across the same images. Figure with permission from Kerth, “Effect of transpiration cooling on boundary layer transition for hypersonic flight,” Ph.D. thesis (University of Oxford, 2022).<sup>42</sup>

coolant on the sensor and its immediate vicinity or whether it holds for the entire boundary layer thickness. Figure 9 suggests the latter. Like Fig. 8, it maps the schlieren PSD along the cone, but now simply at constant heights above the surface. Schlieren spectra indicate second mode activity in a range of roughly 210–260 kHz and between  $x = 360$  and  $x = 400$  mm in good agreement with PCB sensors (left column of the figure). Comparing power spectra maps at  $\bar{y} = 1.2$  and 1.1 mm above the cone evidently shows a drop in spectral power and a downwards shift in frequency distribution when nitrogen is injected. The two upmost pixel rows within the boundary layer thus confirm what has been inferred from surface measurements before.<sup>14</sup> Only the spectral broadening as observed by Camillo *et al.*<sup>14</sup> for nitrogen injection and predicted by Miró *et al.*<sup>90</sup> for helium transpiration does not occur. However, spectral broadening was also not detected by surface sensors on our model for any injection cases.<sup>41,42</sup>

### F. Second mode power distribution across the boundary layer thickness

The plots in Fig. 10 re-iterate the results from the manually selected paths in Sec. III D, where we demonstrated the displacement of second mode power by plotting the spectra of a pixel row along the  $x$ -axis. Here, we select four specific locations along the  $x$ -coordinate and plot the spectra of the respective vertical pixel rows, perpendicular

to the model. An adaptable colormap shows spectral power estimates for the respective frequencies and one can observe changes or dissolution of second mode activity.

For a natural transition case, most of the spectral power is found at or even above the laminar boundary layer height. This is in good agreement with other schlieren spectral analysis results in the field, where second mode oscillations extended up to 150% of the boundary layer height (see, e.g., Laurence *et al.*<sup>91</sup> in Fig. 13).

The fourth quadrant of Fig. 10 shows the case with  $F(\text{He}) = 0.1\%$ . Onset of full turbulence across the entire boundary layer thickness is already observed in the middle of the injector segment at  $x = 312.5$  mm. A chaotic oscillation spectrum exists from the cone edge up to 4 mm above the model surface.

For the helium injection case shown in Fig. 8 ( $F = 0.06\%$ ), the existence of a stable cooling film can be measured. At  $x = 420$  mm (row 4 column 2 in Fig. 10), a turbulent spectrum can be found, however, only above  $\bar{y} \approx 0.8$  mm. A transitioning boundary layer coexists on top of a laminar coolant film. Identifying transition through surface instrumentation may thus be significantly flawed in this case. Those sensors and any transition criteria would correctly detect laminar flow, which however does not represent the state across the whole boundary layer. This presentation also re-iterates the main findings from Fig. 8. As discussed before, it is known that second mode instability waves concentrate on a certain height of a naturally transitioning boundary

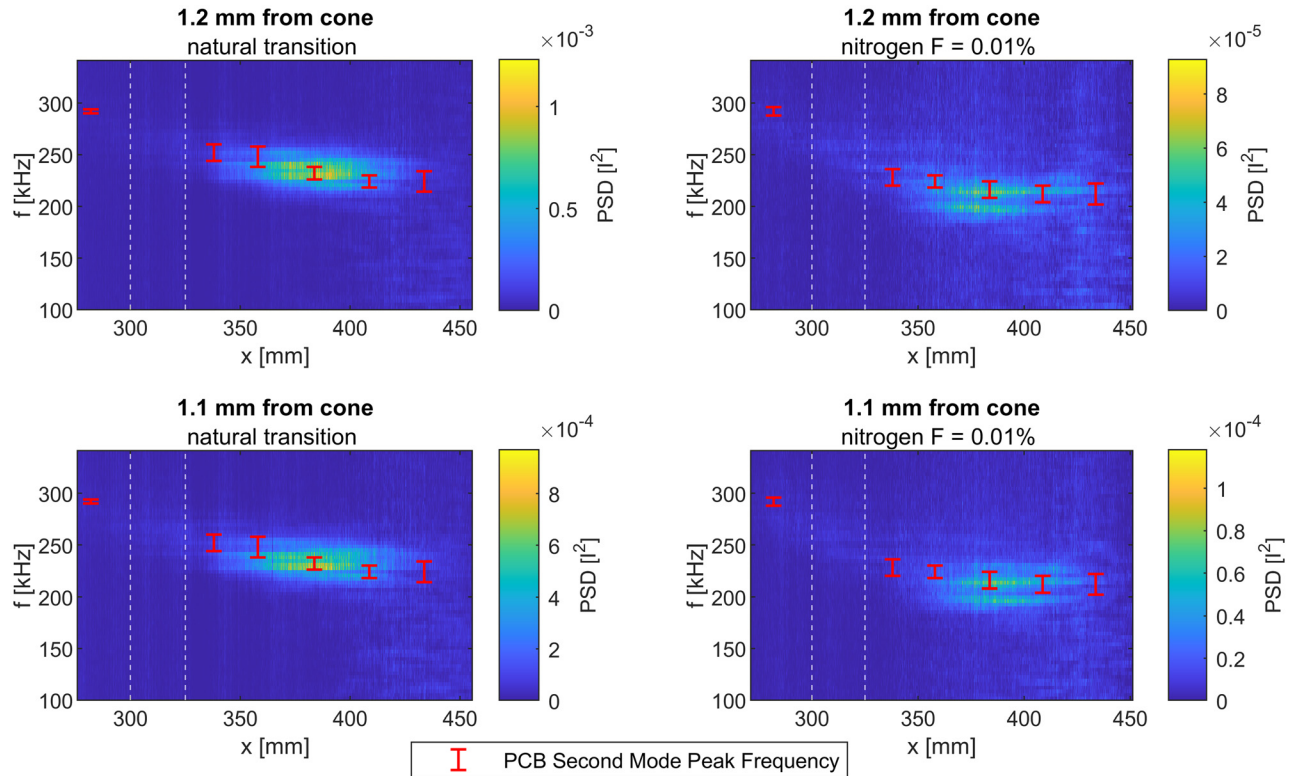


**FIG. 9.** Power spectra maps of schlieren images. PSDs are calculated for each pixel along a path with the given distance from the detected cone edge. The error bars given for the central frequency of the second mode represent the full width at half maximum of the fitted Gaussian distribution. The injector location is marked as a white dashed in the color maps. Figure with permission from Kerth, “Effect of transpiration cooling on boundary layer transition for hypersonic flight,” Ph.D. thesis (University of Oxford, 2022).<sup>42</sup>

layer as seen in schlieren. With helium transpiration cooling, this height changes significantly and extends far beyond the natural boundary-layer profile. This is particularly evident, when comparing the locations  $x = 312.5$  and  $x = 328$  mm for natural transition and  $F(\text{He}) = 0.06\%$ , which are always in one column in Fig. 10.

In addition, this analysis demonstrates evidence for oscillation displacement in two additional cases. For  $F(\text{He}) = 0.1\%$ , the plot at  $x = 328$  mm shows evidence of oscillations displaced beyond  $\bar{y} = 2$  mm. The equivalent with  $F(\text{N}_2) = 0.1\%$  is not nearly as pronounced, but nevertheless, the distribution of spectral power shifts around two pixels away from the cone, while the frequency is largely unaffected.

### 1. FLDI Measurements

FLDI is applied to detect second mode instabilities above the injector. Two locations within and above the undisturbed boundary layer are chosen for the focal point. A lies  $\bar{y}_A = (1.5 \pm 0.2)$  mm and B  $\bar{y}_B = (2.5 \pm 0.2)$  mm above the cone surface, respectively. A is chosen to be at the very end of the visible laminar boundary layer in schlieren at  $x = 312$  mm, which is the middle of the injector segment (see Figs. 1 and 11). Point B lies within the post-shock flow outside of the natural boundary layer. Figure 11 confirms key parts of the previous schlieren-method based findings. It shows the locations of both FLDI

points, the measured spectra for the different injection scenarios for those cases, and the associated PSDs from the respective schlieren pixels. Due to the change of boundary layer profile, FLDI point B lies within a visible density gradient field for helium injection, but not for natural transition. It is now evident from the shown power spectra how the second mode frequency peak can be detected in point B with helium injection, while it cannot be seen with natural transition. Similarly, with point A nearly exceeding the boundary layer height without injection, an increase in second mode power is found with helium injection. Both of those findings are in contrast with the trend inferred from surface instruments downstream of the injector. Those suggest that the second mode power is reduced by gas injection. The bandpower decrease shown in Fig. 5 seems to only hold for the close vicinity of the surface. Helium injection into a developed and growing second mode instability at low enthalpy seems to have little damping or stabilizing effect. At least locally, injection pushes the second mode away from the surface, and it can still be detected further away from the cone. As nitrogen injection does not alter the edge profile of the boundary layer to such an extent, no second mode signal could be detected for point B. It is important to highlight that altering the injection rate or changing the injectant gas results in points A and B being situated at different positions relative to the boundary layer profile. Careful determination of FLDI probe locations is required, based on the expected, or visualized, boundary layer profile, and the practicality

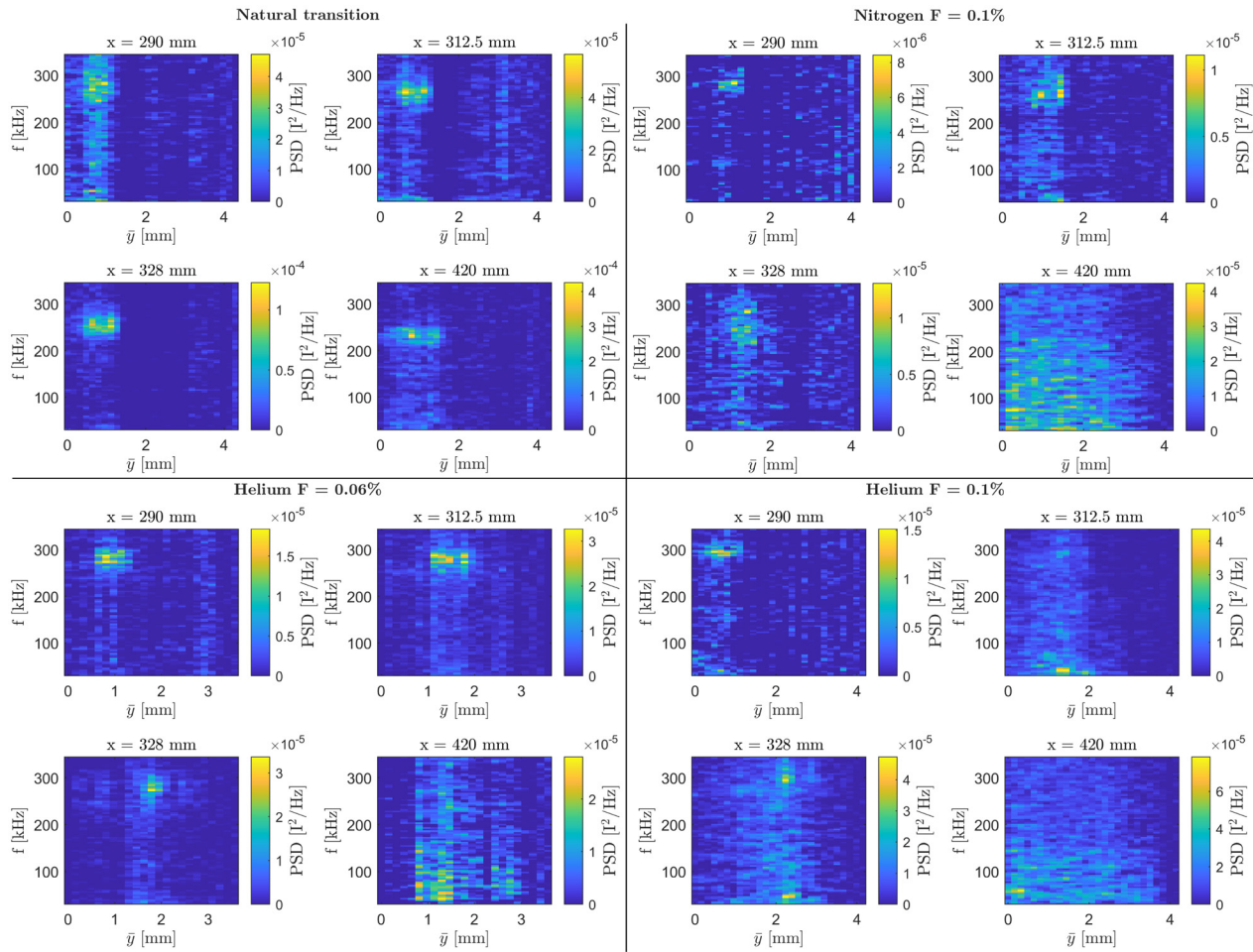


**FIG. 10.** Wall-normal power spectra through boundary layer thickness. The power spectra are plotted for four locations along the transition process. Because the schlieren system was not always aligned to the exact same position,  $\bar{y}$  ranges change across the test cases. The same PSD calculations as for Figs. 9 and 8 were used to generate the plots. Figure with permission from Kerth, “Effect of transpiration cooling on boundary layer transition for hypersonic flight,” Ph.D. thesis (University of Oxford, 2022).<sup>32</sup>

of positioning the FLDI probe location relative to the model surface. Furthermore, it must be highlighted that the comparison of nitrogen to helium injection is based on a mass flux measurement. The definition of  $F$  in this work is based on  $\dot{m}$  and due to the ratio of molecular masses, helium injection yields a seven times higher volumetric flow rate than nitrogen injection at the same  $F$ . Consequently, helium generates much higher film coverage and a larger displacement for the boundary layer profile.

Spectra directly taken for the corresponding pixels in schlieren qualitatively agree with FLDI. Frequency shift and increased band-power can be observed for the comparison in point A. For point B, no sufficient signal was measured by schlieren, as it does not possess the sensitivity of a differential interferometer. To obtain the presented PSDs and uncertainties, the pixels coinciding with the location of the FLDI laser beam were selected. As the adjustment in the  $\bar{y}$ -direction was relatively precise due to the 10  $\mu\text{m}$  steps of the lab jack, the alignment uncertainty is neglected in this coordinate. Nevertheless, due to

the diameter of the laser point, an uncertainty of  $\pm 1$  pixels is assumed. For the  $x$ -direction, alignment was done manually, and hence, the uncertainty is  $\pm 5$  pixels. The error bars are thus obtained by calculating the mean and standard error of PSDs within a rectangle of 33 pixels—11 in the  $\bar{y}$ -direction and 3 in the  $x$ -direction—centered around the FLDI point. To exclude any possible contamination of the PSD through freestream content, the mean PSD of the top pixel row, high above the boundary layer is subtracted from all points, as indicated on the vertical axis of Fig. 11. Negative values were set to 0 as they are nonphysical.

### G. Experimental definition of transition

Previous sections have pointed toward significant ambiguities of standard practice measurements if transition and transpiration cooling are present simultaneously and also disclosed an underlying physical effect. To reach a comprehensive and overarching conclusion, several different techniques to infer transition onset will be presented and assessed with respect to their suitability.

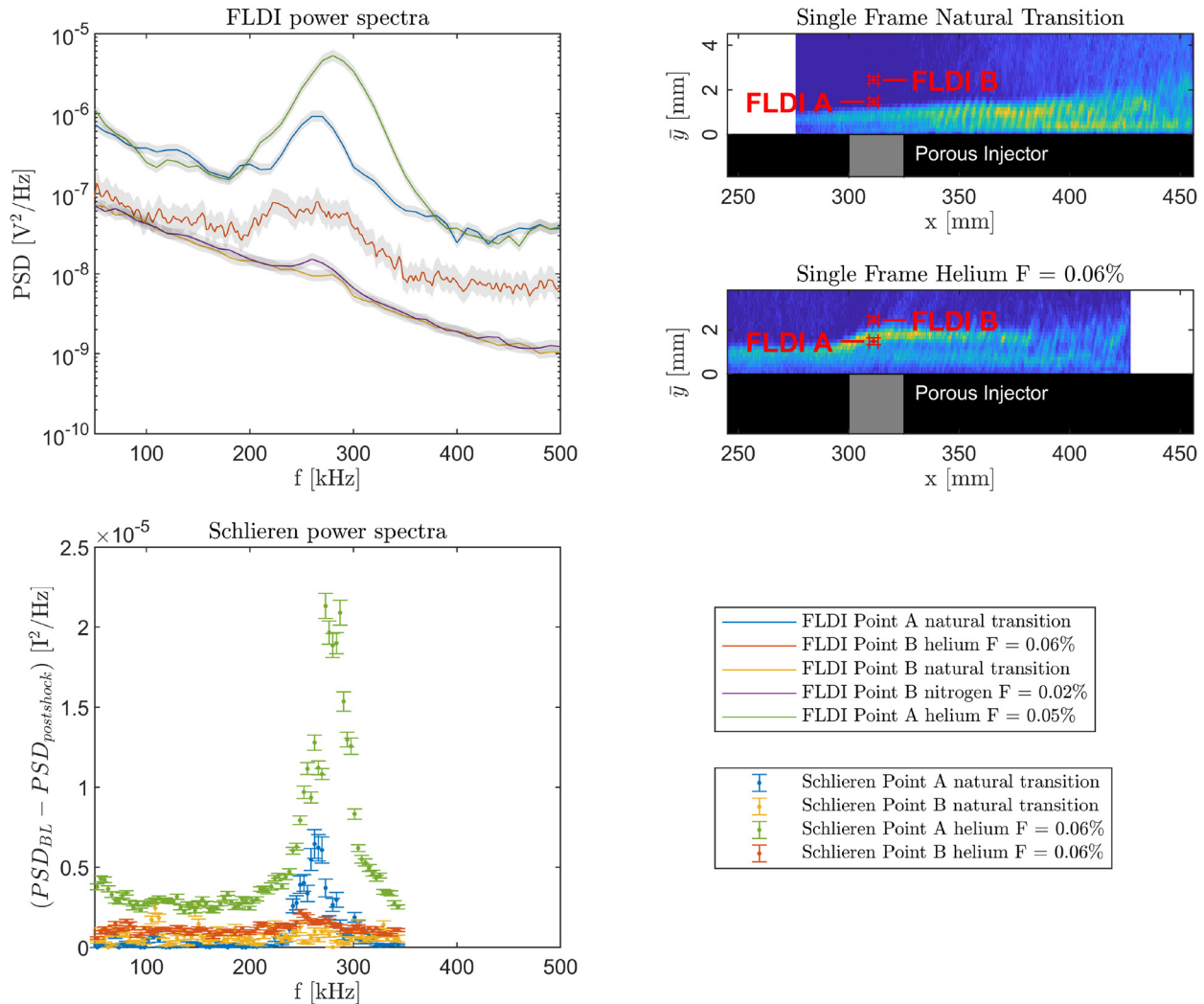


FIG. 11. Both locations above the injector where FLDI was applied are marked in a schlieren image. The error bars do not indicate the size of the FLDI laser point but rather the goodness of reproducible realignment. Figure with permission from Kerth, “Effect of transpiration cooling on boundary layer transition for hypersonic flight,” Ph.D. thesis (University of Oxford, 2022).<sup>42</sup>

1. First thin film gauge

The most upstream heat flux gauge significantly above the laminar Eckert correlation is selected as the transition onset point. Hereby, significant means the Stanton number exceeds the laminar Eckert correlation 68% confidence interval. As an example,  $x_{tr} = 358$  mm for the natural transition case (Fig. 5). This method is obviously flawed when injection or cooling is present, but nevertheless included for completeness.

2. Stanton number linear fit

Similarly to Camillo *et al.*,<sup>14</sup> a linear fit is calculated through the thin film gauge measurements downstream of the local minimum. An example is shown below in Fig. 12. The intersection of the fit and the upper 68% confidence interval threshold of the laminar Eckert correlation is  $x_{tr}$ .

3. Schlieren human input

The schlieren videos from the tunnel tests showed a continuously moving transition front. All spectra and heat transfer values shown are time averages. In order to reproduce this, an experimenter is shown 100 randomly selected post-processed schlieren images like in Fig. 7 from the steady flow test time. The onset of full turbulence is manually selected by clicking on the transition point on every frame. Second modes are not counted as turbulence, only the presence of chaotically fluctuating eddies. The inputs from 100 frames are averaged and used as  $x_{tr}$  (Fig. 13).

4. Schlieren low frequency power

As seen in previously shown spectra, the “irregular disordered”<sup>83</sup> nature of turbulence causes a spread of fluctuations across a large

02 May 2024 12:57:40

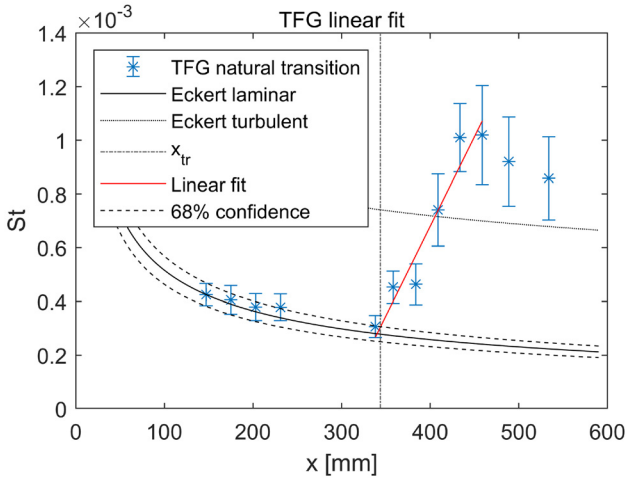


FIG. 12. Linear fit through TFG downstream of heat flux local minimum. Figure with permission from Kerth, "Effect of transpiration cooling on boundary layer transition for hypersonic flight," Ph.D. thesis (University of Oxford, 2022).<sup>42</sup>

frequency spectrum. The increasing presence of frequencies lower than the second mode (i.e., < 100 kHz) is used as a transition criterion. A sum is calculated of all power in this range across the entire available  $\bar{y}$  distance in the schlieren image. Defining  $x_{tr}$  is performed via MATLAB's inbuilt change point detection. The number of change points is set to one, and hence, the function will iteratively subdivide the data into two regions with different statistics with respect to rms values.<sup>92-94</sup>

5. Schlieren time variance

Similarly to the low frequency method, the irregularity of turbulence can be characterized using the time variance of schlieren signals. Once the boundary layer becomes turbulent, an ordered, steady signal from a laminar layer is replaced by chaotic fluctuations in space and time. To eliminate random fluctuations of the pixels in the camera sensor, schlieren images are down sampled by a factor of 1/3. The time variance is calculated for every pixel and normalized by the averaged pixel intensity. The variances are summed up in the  $\bar{y}$  direction. Using

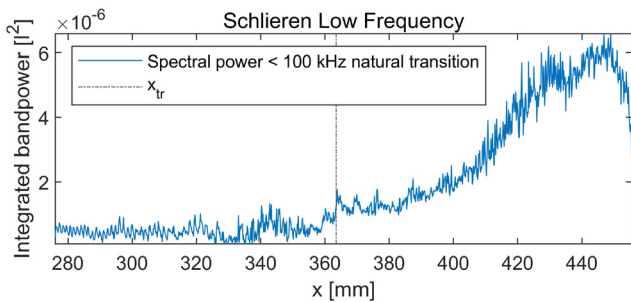


FIG. 13. Schlieren low frequency power criterion. Figure with permission from Kerth, "Effect of transpiration cooling on boundary layer transition for hypersonic flight," Ph.D. thesis (University of Oxford, 2022).<sup>42</sup> with permission.

MATLAB's change point detection,  $x_{tr}$ , is determined as for the low frequency method.

6. Summary of transition locations

Locations for all methods are shown for four test cases in Table IV. Some differences in transition location can be addressed to the role of instability growth. While the heat flux based methods are most likely triggered by amplified second modes, the schlieren based methods were not. The latter techniques identify the end of transition, while the former detect the onset.<sup>3</sup> Notably, no schlieren criterion indicates a transition delay for any injection scenario. Furthermore, optical techniques always showed a reduction in spectral power for boundary layer oscillations for all injection cases, provided that oscillations could still be measured. Less power is observed in frequency spectra across the entire boundary layer thickness, but the remaining power seems to be effectively displaced from the cone surface. While the growth of eigenmodes can be reduced, altered or interrupted, it seems like by-pass mechanisms still cause fluid turbulence to shift upstream.<sup>81,85</sup>

The compared methods are only a subset of those available in the literature (see, e.g., Pate<sup>22</sup>) for a summary. Some of those mentioned, for example, measurements of increasing boundary layer thickness would not be applicable to gas injection cases. Others, like measurements of Pitot pressure or examinations of surface oil patterns, may suffer from the same inaccuracy as the surface instrumentation presented here.

IV. DISCUSSION

Many of the key results from Camillo *et al.*<sup>14</sup> could be confirmed qualitatively with the present investigation. Nitrogen injection leads to a reduction in second mode power, which held across the entire boundary layer thickness. While this led to an earlier onset of full turbulence, surface heat flux values remained below an uncooled laminar Eckert correlation for an extended distance. This paper has re-iterated the results from older research articles, that any conclusions from this comparison about the fluid mechanical state of the boundary-layer flowfield are meaningless. However, the evaluation of wall heat fluxes and their comparison to Eckerts criteria may still be of interest to vehicle designers, when choosing a cooling technique or adequate material. A comparison of high frequency pressure and heat flux can hereby show how cooling must be the primary reason for such a delay in heat transfer rise. Power spectra reached fully turbulent values earlier than

TABLE IV. Summary of transition locations.

F (%) Method	Coolant				
	None	Helium		Nitrogen	
	0	0.04	0.1	0.01	0.17
	$x_{tr}$ (mm)				
Schlieren human input	431.6	378.6	324.7	419.4	388.3
Schlieren low frequency power	363.5	341.5	303.2	354.1	342.6
Schlieren time variance	398.5	345.4	299.1	388.4	341.2
TFG fit	339.6	387.4	382.1	354.9	355.5
First TFG	358	433.7	408.7	383.7	383.7



without injection. Schlieren hereby confirms how the boundary layer maintained its shape across the injector. From a heat transfer perspective, helium injection yields the same results. Furthermore, it caused a relative reduction in heat transfer all the way until a fully turbulent level is reached.

When considering the instability mechanism, helium cooling shows different behavior: First, disruption to the boundary layer profile is visible in schlieren images, and second, its thickness grows by almost a factor of two and full turbulence can be observed in schlieren where neither of the surface instruments would suggest its presence. The boundary layer thickening can be ascribed to the low molecular mass and high thermal diffusivity<sup>90</sup> of helium, which has been previously reported,<sup>24</sup> analytically predicted,<sup>88</sup> and numerically investigated.<sup>89</sup> A heated boundary layer gas is displaced effectively from the surface, resulting in low or no detection of skin friction, or density oscillations by sensors. Upon turbulent mixing, this diminishes slowly due to the high thermal diffusivity of helium. Naved *et al.*<sup>39</sup> discovered that helium exhibits a cooling efficiency 16 times greater than nitrogen in turbulent flow. This exceptional suitability of helium also stems from its thermal properties, such as the heat capacity,<sup>24</sup> and recent numerical investigations have also shown that said thermophysical properties may also influence the effect of helium injection on boundary-layer stability.<sup>90</sup>

It is now evident why surface measurements with helium injection also inadequately represent the transition mechanism. Density fluctuation spectra obtained from schlieren and FLDI revealed the persistence of the second mode instability above the surface. This observation raises two possible interpretations: either instability damping occurs solely at the surface, or the air boundary layer is displaced away from the measurement sensors together with the second mode oscillation waves. Helium transpiration not only displaces the hot boundary layer gas but also appears to affect the instability waveguide. Apart from the fluid mechanical disturbance induced by gas injection, there exists an instability mechanism, although it is not localized at the surface.

Although numerous instances were observed where a net reduction in surface heat flux along the model was measured, we refrain from asserting stabilization. In certain helium transpiration scenarios, extended periods of laminar or sub-laminar surface heat flux were evident. However, optical methods showcased either turbulent behavior or evolving transition mechanisms in the same area. The case with Helium injection at  $F = 0.1\%$  shows transition already within the injector patch, as clearly visible in schlieren images. At this injection rate, helium seems to create a significant fluidic obstacle for the incoming boundary layer flow, due to its high volume. Instabilities, or an intermediate transitional phase could not be identified, and transpiration rather acts as an immediate trip for the boundary layer.

Moreover, a quantifiable displacement was observed within a narrow range of helium blowing ratios, spanning from  $F = 0.04\%$  to  $F = 0.06\%$ . When injecting a significantly higher percentage ( $F = 0.1\%$ ), some instability wave displacement occurred (refer to row 4, column 3 of Fig. 10), but primarily led to transition movement upstream. Nitrogen injection at  $F = 0.1\%$  also exhibited some displacement, although not as prominently as in the helium cases. Consequently, the alteration in the boundary layer profile was less observable in these instances.

## V. CONCLUSIONS

Difficulties to experimentally assess boundary-layer transition under the influence of transpiration cooling are well known. Further fluid mechanical insight is however required, so those two effects can be fully decoupled in the future. We used a  $7^\circ$  half-angle cone model in a low enthalpy Mach 7 facility, to study direct interactions of hypersonic transition and gas injection in the close vicinity of a porous injector.

At sufficiently low rates, injection of helium or nitrogen was found to delay a rise of surface heat transfer levels above a laminar correlation. Notably, helium injection reduced surface heat fluxes significantly stronger than nitrogen, in line with many other studies in the field. Helium injection caused reduced rates of surface heat flux, while schlieren images already showed turbulent behavior at the same location. The cooling film created by helium has a strong impact on the boundary layer geometry. As shown by schlieren and FLDI measurements, the instability mechanism moves away from the surfaces but keeps existing for a certain range of blowing ratios where the effect is large enough to be observable, but transpiration is sufficiently limited to not trip the boundary layer. We report that second mode oscillations can be displaced beyond the original boundary layer waveguide through foreign gas injection into growing instability waves. Nevertheless, schlieren images demonstrated an earlier onset of turbulence than without any injection. While instabilities and turbulence are no longer present at the surface, they still occur.

Surface pressure and heat transfer methods were critically assessed. They are insufficient in capturing the boundary layer stability state with downstream injection. The coolant film influences those sensors, impairing their signal's meaningfulness for the rest of the boundary layer. Information in the direct vicinity of the model surface is still invaluable and necessary for any investigation in hypersonic flow. Dependency on the distance from the model surface of several parameters necessitates the use of non-intrusive optical techniques such as schlieren to complement surface instruments, as also noted by other studies. Especially the finding about displacing modal oscillations may improve the fundamental understanding of hypersonic instability and transition behavior with coolant transpiration. It furthermore informs future simulation efforts in the field about stability, coolant film coverage, or mixing models.

## ACKNOWLEDGMENTS

We acknowledge the EPSRC Transpiration Cooling grant (No. EP/P000878/1). Thank you for enabling Hypersonic Transpiration Cooling research at the University of Oxford. We would also like to acknowledge our workshop technicians David O'Dell, Duncan Blake, Harry Kachika, and Leon Blake for machining the test model. In addition, we thank Andrea Dabija and Liam Boland for their work on surface instrumentation. Thank you to Tristan Crumpton for running the HDT. The first author would also like to thank his fellow Ph.D. student colleagues Alex Glenn and Joe Steer for their patience. Two different wind tunnels operated in the same room at the same time. Every time the FLDI laser had to be aligned you had to leave the room and interrupt your work on T6. Thank you for being so considerate.

## AUTHOR DECLARATIONS

### Conflict of Interest

The authors have no conflicts to disclose.

### Author Contributions

**Philipp Kerth:** Investigation (equal). **Laurent M. Le Page:** Investigation (equal). **Sebastien Wylie:** Data curation (lead). **Raghul Ravichandran:** Methodology (lead). **Andrew Ceruzzi:** Formal analysis (equal). **Ben Williams:** Supervision (lead). **Matthew McGilvray:** Supervision (lead).

### DATA AVAILABILITY

The data that support the findings of this study will be made openly available via the Oxford Research Archive after publication of the manuscript.

### REFERENCES

- <sup>1</sup>E. Reshotko, "Transition issues for atmospheric entry," *J. Spacecr. Rockets* **45**, 161–164 (2008).
- <sup>2</sup>C. B. Johnson, P. C. Stainback, K. C. Wicker, and L. R. Boney, "Boundary-layer edge conditions and transition Reynolds number data for a flight test at Mach 20 (Reentry F)," Technical Report No. NASA-TM-X-2584 (NASA, 1972).
- <sup>3</sup>C. J. Stalmach, Jr., J. J. Bertin, T. C. Pope, and M. H. McCloskey, "A study of boundary layer transition on outgassing cones in hypersonic flow," Technical Report No. NASA-CR-1908 (NASA, 1971).
- <sup>4</sup>S. P. Schneider, "Hypersonic laminar-turbulent transition on circular cones and scramjet forebodies," *Prog. Aerosp. Sci.* **40**, 1–50 (2004).
- <sup>5</sup>S. P. Schneider, "Development of hypersonic quiet tunnels," *J. Spacecr. Rockets* **45**, 641–664 (2008).
- <sup>6</sup>S. P. Schneider, "Effects of high-speed tunnel noise on laminar-turbulent transition," *J. Spacecr. Rockets* **38**, 323–333 (2001).
- <sup>7</sup>E. R. V. Driest, "The problem of aerodynamic heating," *Aeronaut. Eng. Rev.* **15**, 26–41 (1956).
- <sup>8</sup>G. Grossir, "Longshot hypersonic wind tunnel flow characterization and boundary layer stability investigations," Ph.D. thesis (Von Karman Institute for Fluid Dynamics—Université Libre de Bruxelles, 2015).
- <sup>9</sup>I. Naved, T. Hermann, M. McGilvray, M. Ewenz Rocher, C. Hambidge, L. Doherty, L. Le Page, M. Grossman, and L. Vandeperre, "Heat transfer measurements of a transpiration-cooled stagnation point in transient hypersonic flow," *J. Thermophys. Heat Transfer* **37**, 296–308 (2023).
- <sup>10</sup>F. M. Miró, P. Dehairs, F. Pinna, M. Gkolia, D. Masutti, T. Regert, and O. Chazot, "Effect of wall blowing on hypersonic boundary-layer transition," *AIAA J.* **57**, 1567–1578 (2019).
- <sup>11</sup>J. S. Jewell, "Boundary-layer transition on a slender cone in hypervelocity flow with real gas effects," Ph.D. thesis (California Institute of Technology, 2014).
- <sup>12</sup>F. K. Owen and C. C. Horstman, "Hypersonic transitional boundary layers," *AIAA J.* **10**, 769–775 (1972).
- <sup>13</sup>D. J. Wise and M. K. Smart, "Roughness-induced transition of hypervelocity boundary layers," *J. Spacecr. Rockets* **51**, 847–854 (2014).
- <sup>14</sup>G. P. Camillo, A. Wagner, C. Dittert, L. Benjamin, V. Wartemann, J. Neumann, and R. Hink, "Experimental investigation of the effect of transpiration cooling on second mode instabilities in a hypersonic boundary layer," *Exp. Fluids* **61**, 162 (2020).
- <sup>15</sup>M. A. Kegerise and S. J. Rufer, "Unsteady heat-flux measurements of second-mode instability waves in a hypersonic flat-plate boundary layer," *Exp. Fluids* **57**, 130 (2016).
- <sup>16</sup>L. Paquin, "Effect of cooling on hypersonic Boundary-Layer stability," Ph.D. thesis (University of Maryland, College Park, 2022).
- <sup>17</sup>K. Stetson, R. Kimmel, J. Donaldson, and L. Siler, "A comparison of planar and conical boundary layer stability and transition at a Mach number of 8," AIAA Paper No. AIAA 1991-1639, 1991.
- <sup>18</sup>K. F. Stetson and R. L. Kimmel, "Example of second-mode instability dominance at a Mach number of 5.2," *AIAA J.* **30**, 2974–2976 (1992).
- <sup>19</sup>J. E. LaGraff, "Observations of hypersonic boundary-layer transition using hot wire anemometry," *AIAA J.* **10**, 762–769 (1972).
- <sup>20</sup>D. Berridge, K. Casper, S. Rufer, C. Alba, D. Lewis, S. Beresh, and S. Schneider, "Measurements and computations of second-mode instability waves in several hypersonic wind tunnels," AIAA Paper No. AIAA 2010-5002, 2010.
- <sup>21</sup>M. Estorf, R. Radespiel, S. Schneider, H. Johnson, and S. Hein, "Surface-pressure measurements of second-mode instability in quiet hypersonic flow," AIAA Paper No. AIAA 2008-1153, 2008.
- <sup>22</sup>S. R. Pate, "Dominance of radiated aerodynamic noise on boundary-layer transition in supersonic-hypersonic wind tunnels. Theory and application," Technical Report No. AEDC-TR-77-107 (Arnold Engineering Development Center, Arnold Air Force Station, Tennessee, 1978).
- <sup>23</sup>J. J. Bertin and R. M. Cummings, "Critical hypersonic aerothermodynamic phenomena," *Annu. Rev. Fluid Mech.* **38**, 129 (2006).
- <sup>24</sup>A. Gülhan and S. Braun, "An experimental study on the efficiency of transpiration cooling in laminar and turbulent hypersonic flows," *Exp. Fluids* **50**, 509–525 (2011).
- <sup>25</sup>S. P. Schneider, "Hypersonic boundary-layer transition with ablation and blowing," *J. Spacecr. Rockets* **47**, 225–237 (2010).
- <sup>26</sup>M. W. Rubesin, "The influence of surface injection on heat-transfer and skin friction associated with the high-speed turbulent boundary layer," Technical Report No. NACA-RM-A55L13 (NASA Ames Aeronautical Lab, Moffett Field, CA, 1956).
- <sup>27</sup>T. Hermann, M. McGilvray, and I. Naved, "Performance of transpiration-cooled heat shields for reentry vehicles," *AIAA J.* **58**, 830–841 (2020).
- <sup>28</sup>H. Tanno, T. Komuro, K. Itoh, M. Kuhn, I. Petkov, and B. Esser, "Transpiration cooling experiments in free-piston shock tunnel HIEST," in 8th European Workshop on Thermal Protection Systems and Hot Structures, 2016.
- <sup>29</sup>C. C. Pappas and A. F. Okuno, "Measurements of skin friction of the compressible turbulent boundary layer on a cone with foreign gas injection," *J. Aerosp. Sci.* **27**, 321–333 (1960).
- <sup>30</sup>J. C. Dunavant and P. E. Everhart, "Explorator heat-transfer measurements at Mach 10 on a 7.5 deg total-angle cone downstream of a region of air and helium transpiration cooling," Technical Report No. NASA-TN-D-5554 (NASA, 1969).
- <sup>31</sup>J. Jewell, I. Leyva, N. J. Parziale, and J. E. Shepherd, "Effect of gas injection on transition in hypervelocity boundary layers," in *Proceedings of the 28th International Symposium on Shock Waves* (Springer, 2012), pp. 735–740.
- <sup>32</sup>I. Leyva, S. Laurence, A. Beierholm, H. Hornung, R. Wagnild, and G. Candler, "Transition delay in hypervelocity boundary layers by means of CO<sub>2</sub>/acoustic instability interactions," AIAA Paper No. AIAA 2009-1287, 2009.
- <sup>33</sup>R. Narasimha, "The laminar-turbulent transition zone in the boundary layer," *Prog. Aerosp. Sci.* **22**, 29–80 (1985).
- <sup>34</sup>P. Kerth, R. Ravichandran, A. Pilkington, H. Saad Ifti, S. Wylie, and M. McGilvray, "Hypersonic boundary layer stabilization by helium injection," unpublished (2022).
- <sup>35</sup>A. Wagner, K. Hannemann, and M. Kuhn, "Ultrasonic absorption characteristics of porous carbon-carbon ceramics with random microstructure for passive hypersonic boundary layer transition control," *Exp. Fluids* **55**, 1750 (2014).
- <sup>36</sup>S. P. Schneider, "Effects of roughness on hypersonic boundary-layer transition," *J. Spacecr. Rockets* **45**, 193–209 (2008).
- <sup>37</sup>A. Laganelli and A. Martellucci, "Downstream effects of gaseous injection through a porous nose," AIAA Paper No. AIAA 1972-185, 1972.
- <sup>38</sup>J. G. Marvin and C. M. Akin, "Combined effects of mass addition and nose bluntness on boundary-layer transition," *AIAA J.* **8**, 857–863 (1970).
- <sup>39</sup>I. Naved, T. Hermann, C. Hambidge, H. Saad Ifti, C. Falsetti, M. McGilvray, I. S. Tirichenko, and L. Vandeperre, "Transpiration-cooling heat transfer experiments in laminar and turbulent hypersonic flows," *J. Thermophys. Heat Transfer* **37**, 281–295 (2023).
- <sup>40</sup>H. S. Ifti, "Transpiration cooling of a hypersonic vehicle," Ph.D. thesis (University of Oxford, 2022).
- <sup>41</sup>P. Kerth, S. Wylie, R. Ravichandran, and M. McGilvray, "Gas injection into second mode instability on a 7 degree Cone at Mach 7," AIAA Paper No. AIAA 2022-3856, 2022.
- <sup>42</sup>P. Kerth, "Effect of transpiration cooling on boundary layer transition for hypersonic flight," Ph.D. thesis (University of Oxford, 2022).
- <sup>43</sup>M. Hayne, "The manufacture and mounting of thin film gauges for heat transfer," Report SID-61-275 (University of Queensland Department of Mechanical Engineering, St. Lucia, Australia, 2003).
- <sup>44</sup>M. Collins, K. Chana, and T. Povey, "New technique for the fabrication of miniature thin film heat flux gauges," *Meas. Sci. Technol.* **26**, 025303 (2015).
- <sup>45</sup>S. Wylie, "Hypersonic boundary layer instability measurements at low and high angles of attack," Ph.D. thesis (University of Oxford, 2020).

- <sup>46</sup>Portec, see <https://www.portec.ch/> and <https://toolingtechgroup.com/wp-content/uploads/2018/12/1-metapor-BF100-Data-Sheet.pdf> for “Metapore Porous Materials (2022)” (accessed November 16, 2022).
- <sup>47</sup>T. LLC, see <https://www.portec.ch/> and <https://toolingtechgroup.com/wp-content/uploads/2018/12/1-metapor-BF100-Data-Sheet.pdf> for “Metapor bf100 Al—Air Permeable Material” (accessed November 16, 2022).
- <sup>48</sup>H. S. Ifti, T. Hermann, and M. McGilvray, “Flow characterisation of transpiring porous media for hypersonic vehicles,” AIAA Paper No. AIAA 2018-5167, 2018.
- <sup>49</sup>J. A. Nelder and R. Mead, “A simplex method for function minimization,” *Comput. J.* **7**, 308–313 (1965).
- <sup>50</sup>T. Ishimatsu and E. Morishita, “Taylor-Maccoll hypervelocity analytical solutions,” *Trans. Jpn. Soc. Aeronaut. Space Sci.* **48**, 46–48 (2005).
- <sup>51</sup>G. I. Taylor and J. W. Maccoll, “The air pressure on a cone moving at high speeds. II,” *Proc. R. Soc. Ser. A* **139**, 298–311 (1933).
- <sup>52</sup>C. Dittert, M. Selzer, and H. Böhrk, “Flowfield and pressure decay analysis of porous cones,” *AIAA J.* **55**, 874–882 (2017).
- <sup>53</sup>P. Welch, “The use of fast Fourier transform for the estimation of power spectra: A method based on time averaging over short, modified periodograms,” *IEEE Trans. Audio Electroacoust.* **15**, 70–73 (1967).
- <sup>54</sup>A. V. Oppenheim, *Discrete-Time Signal Processing* (Pearson Education India, 1999).
- <sup>55</sup>M. L. G. Oldfield, “Impulse response processing of transient heat transfer gauge signals,” *J. Turbomach.* **130**, 021023 (2008).
- <sup>56</sup>E. R. G. Eckert and J. N. B. Livingood, “Comparison of effectiveness of convection-, transpiration-, and film-cooling methods with air as coolant,” Technical Report No. NACA-TN-3010 (Lewis Flight Propulsion Laboratory, Cleveland, Ohio, 1954).
- <sup>57</sup>T. H. Chilton and A. P. Colburn, “Mass transfer (absorption) coefficients prediction from data on heat transfer and fluid friction,” *Ind. Eng. Chem.* **26**, 1183–1187 (1934).
- <sup>58</sup>L. F. Crabtree, R. L. Dommert, and J. G. Woodley, “Estimation of heat transfer to flat plates, cones and blunt bodies,” Technical Report No. R & M 3637 (Ministry of Technology, Aeronautical Research Council, 1965).
- <sup>59</sup>H. Ludwig, “Der rohrwindkanal,” *Z. Flugwiss.* **3**, 206–216 (1955).
- <sup>60</sup>M. McGilvray, L. J. Doherty, A. J. Neely, R. Pearce, and P. Ireland, “The oxford high density tunnel,” AIAA Paper No. AIAA 2015-3548, 2015.
- <sup>61</sup>S. Wylie, L. Doherty, and M. McGilvray, “Commissioning of the oxford high density tunnel (HDT) for boundary layer instability measurements at Mach 7,” AIAA Paper No. AIAA 2018-3074, 2018.
- <sup>62</sup>T. Hermann, M. McGilvray, C. Hambidge, L. Doherty, and D. Buttsworth, “Total temperature measurements in the oxford high density tunnel,” in *International Conference on Flight Vehicles, Aerothermodynamics and Re-Entry Missions and Engineering (FAR)* (European Space Agency, 2019).
- <sup>63</sup>F. Keyes, “A summary of viscosity and heat-conduction data for He, A, H<sub>2</sub>, O<sub>2</sub>, N<sub>2</sub>, CO, CO<sub>2</sub>, H<sub>2</sub>O, and Air,” *J. Fluids Eng.* **73**, 589–595 (1951).
- <sup>64</sup>F. G. Keyes, “The heat conductivity, viscosity, specific heat and Prandtl numbers for thirteen gases,” Technical Report No. NSA-07-004618 (Massachusetts Institute of Technology, Cambridge, 1952).
- <sup>65</sup>M. Versluis, “High-speed imaging in fluids,” *Exp. Fluids* **54**, 1458 (2013).
- <sup>66</sup>G. S. Settles and M. J. Hargather, “A review of recent developments in schlieren and shadowgraph techniques,” *Meas. Sci. Technol.* **28**, 042001 (2017).
- <sup>67</sup>M. R. Fulghum, “Turbulence measurements in high-speed wind tunnels using focusing laser differential interferometry,” Ph.D. thesis (The Pennsylvania State University, 2014).
- <sup>68</sup>G. Smeets, “Laser interferometer for high sensitivity measurements on transient phase objects,” *IEEE Trans. Aerosp. Electron. Syst.* **AES-8**, 186–190 (1972).
- <sup>69</sup>B. E. Schmidt and J. E. Shepherd, “Analysis of focused laser differential interferometry,” *Appl. Opt.* **54**, 8459–8472 (2015).
- <sup>70</sup>N. Parziale, J. Shepherd, and H. Hornung, “Differential interferometric measurement of instability in a hypervelocity boundary layer,” *AIAA J.* **51**, 750–754 (2013).
- <sup>71</sup>A. Ceruzzi, “Development of two-point focused laser differential interferometry for applications in high-speed wind tunnels,” Ph.D. thesis (University of Maryland, 2022).
- <sup>72</sup>H. Sun, *Basic Optical Engineering for Engineers and Scientists (Press Monographs)* (SPIE Press, Bellingham, Washington, 2019).
- <sup>73</sup>G. S. Settles, *Schlieren and Shadowgraph Techniques: Visualizing Phenomena in Transparent Media* (Springer Science & Business Media, 2001).
- <sup>74</sup>A. P. Ceruzzi and C. P. Cadou, “Interpreting single-point and two-point focused laser differential interferometry in a turbulent jet,” *Exp. Fluids* **63**, 112 (2022).
- <sup>75</sup>MathWorks, see <https://uk.mathworks.com/help/images/ref/checkerboard.html> for “Checkerboard—Create Checkerboard Image (2022)” (accessed January 4, 2023).
- <sup>76</sup>E. K. Benitez, M. P. Borg, J. L. Hill, M. T. Aultman, L. Duan, C. L. Running, and J. S. Jewell, “Quantitative focused laser differential interferometry with hypersonic turbulent boundary layers,” *Appl. Opt.* **61**, 9203–9216 (2022).
- <sup>77</sup>E. K. Benitez, M. P. Borg, C. Rhodes, and J. S. Jewell, “Optical-axis spatial sensitivity of a simulated focused laser differential interferometer,” *AIAA J.* **61**, 1925–1938 (2023).
- <sup>78</sup>N. J. Parziale, J. E. Shepherd, and H. G. Hornung, “Free-stream density perturbations in a reflected-shock tunnel,” *Exp. Fluids* **55**, 1665 (2014).
- <sup>79</sup>G. I. Gillespie, A. P. Ceruzzi, and S. J. Laurence, “A multi-point focused laser differential interferometer for characterizing freestream disturbances in hypersonic wind tunnels,” *Exp. Fluids* **63**, 180 (2022).
- <sup>80</sup>J. M. Lawson, M. C. Neet, I. J. Grossman, and J. M. Austin, “Static and dynamic characterization of a focused laser differential interferometer,” *Exp. Fluids* **61**, 187 (2020).
- <sup>81</sup>A. Fedorov, “Transition and stability of high-speed boundary layers,” *Annu. Rev. Fluid Mech.* **43**, 79–95 (2011).
- <sup>82</sup>L. M. Mack, “Boundary-layer linear stability theory,” Technical Report No. AGARD 709 (California Institute of Technology, Pasadena Jet Propulsion Laboratory, 1984).
- <sup>83</sup>L. D. Landau and E. M. Lifshitz, *Fluid Mechanics: Landau and Lifshitz: Course of Theoretical Physics* (Elsevier, 2013), Vol. 6.
- <sup>84</sup>A. V. Fedorov, V. Soudakov, and I. A. Leyva, “Stability analysis of high-speed boundary-layer flow with gas injection,” AIAA Paper No. AIAA 2014-2498, 2014.
- <sup>85</sup>M. V. Morkovin, “Transition in open flow systems—a reassessment,” *Bull. Am. Phys. Soc.* **39**, 1882 (1994).
- <sup>86</sup>E. Reshotko, “Transient growth: A factor in bypass transition,” *Phys. Fluids* **13**, 1067–1075 (2001).
- <sup>87</sup>B. E. Schmidt, “On the stability of supersonic boundary layers with injection,” Ph.D. thesis (California Institute of Technology, 2016).
- <sup>88</sup>H. S. Ifti, T. Hermann, and M. McGilvray, “Analytical model of transpired-coolant concentration at downstream wall in high-speed laminar flow,” *AIAA J.* **61**, 3541–3510 (2023).
- <sup>89</sup>H. S. Ifti, T. Hermann, M. McGilvray, and J. Merrifield, “Numerical simulation of transpiration cooling in a laminar hypersonic boundary layer,” *J. Spacecr. Rockets* **59**, 1726–1735 (2022).
- <sup>90</sup>F. M. Miró and F. Pinna, “Injection-gas-composition effects on hypersonic boundary-layer transition,” *J. Fluid Mech.* **890**, R4 (2020).
- <sup>91</sup>S. Laurence, A. Wagner, and K. Hannemann, “Experimental study of second-mode instability growth and breakdown in a hypersonic boundary layer using high-speed schlieren visualization,” *J. Fluid Mech.* **797**, 471–503 (2016).
- <sup>92</sup>MathWorks, see <https://uk.mathworks.com/help/signal/ref/findchangepts.html> for “Findchangepts—Find Abrupt Changes in Signals (2022)” (accessed November 17, 2021).
- <sup>93</sup>R. Killick, P. Fearnhead, and I. A. Eckley, “Optimal detection of changepoints with a linear computational cost,” *J. Am. Stat. Assoc.* **107**, 1590–1598 (2012).
- <sup>94</sup>M. Lavielle, “Using penalized contrasts for the change-point problem,” *Signal Process.* **85**, 1501–1510 (2005).